



A local to national-scale inverse modeling system to assess the potential of spaceborne CO₂ measurements for the monitoring of anthropogenic emissions

Diego Santaren¹, Grégoire Broquet¹, François-Marie Bréon¹, Frédéric Chevallier¹, Denis Siméoni²,
5 Philippe Ciais¹

¹Laboratoire des Sciences du Climat et de l'Environnement, CEA-CNRS-UVSQ, Gif-sur-Yvette, France

²Thales Alenia Space, La Bocca, France

Correspondence to: Diego Santaren (diegosantaren@gmail.com)

Abstract. This work presents a flux inversion system for assessing the potential of new satellite imagery measurements of
10 atmospheric CO₂ to monitor anthropogenic emissions at scales ranging from local intense point sources to regional and
national scales. While the modeling framework keeps the complexity of previous studies focused on individual and large
cities, this system encompasses a wide range of sources to extend the scope of the analysis. This atmospheric inversion
system uses a zoomed configuration of the regional transport model CHIMERE which covers most of Western Europe with a
2-km resolution grid over Northern France, Western Germany and Benelux. For each day of March and May 2016, over the
15 6 hours before a given satellite overpass, the inversion controls separately the hourly budgets of anthropogenic emissions in
this area from ~300 cities, power plants and regions. The inversion also controls hourly regional budgets of the natural
fluxes. This enables the analysis of results at the local to regional scales for a wide range of sources in terms of emission
budgets and spatial extent while accounting for the uncertainties associated with natural fluxes and the overlapping of
plumes from different sources. The potential of satellite data to monitor CO₂ fluxes is quantified by posterior uncertainties or
20 uncertainty reductions (URs) from prior inventory-based statistical knowledge.

A first analysis focuses on the hourly to 6-hour budgets of the emissions of the Paris urban area, and on the sensitivity of the
results to different characteristics of the images of vertically integrated CO₂ (XCO₂) corresponding to the spaceborne
instrument: the pixel spatial resolution, the precision of the XCO₂ retrievals per pixel, and the swath width. This sensitivity
analysis provides a correspondence between these parameters and thresholds on the targeted precisions on emission
25 estimates. However, the results indicate a large sensitivity to the wind speed and to the *prior* flux uncertainties. The analysis
is then extended to the large ensemble of point sources, cities and regions in the study domain, with a focus on the inversion
system ability to monitor separately neighbor sources whose atmospheric signatures overlap and are also mixed with those
produced by natural fluxes. Results highlight the strong dependence of uncertainty reductions to the emission budgets, to the
wind speed and whether the focus is on point or area sources. With the system hypothesis that the atmospheric transport is
30 perfectly known, the results indicate that the atmospheric signal overlap is not a critical issue. For the emissions within the 6-
hours before a satellite overpass, UR of more than 50% can only be achieved for power plants and cities whose annual



emissions are more than $\sim 2 \text{ MtC}\cdot\text{yr}^{-1}$. For more regional budgets encompassing more diffuse emissions, this threshold increases up to $\sim 10 \text{ MtC}\cdot\text{yr}^{-1}$. The results suggest therefore an imbalance of the monitoring capabilities towards high and dense sources.

35 1. Introduction

Comprehensive information about anthropogenic CO_2 emissions integrated at the scale of power plants, cities, regions and countries up to the globe would allow decision makers to track the effectiveness of emission reduction policies in the context of the Paris Agreement on Climate and other voluntary emission reduction efforts. By observing the CO_2 plumes downwind of large cities and industrial plants, and atmospheric signals at a few to several hundred km scales, future high-resolution
40 spectro-imagery of the column-average CO_2 dry air mole fraction (XCO_2) may help addressing this need (Ciais et al., 2015; Pillai et al., 2016; Pinty et al., 2017; Schwandner et al., 2017; Broquet et al., 2018). The Copernicus Anthropogenic Carbon Dioxide Monitoring mission (CO2M, (Pinty et al., 2017)) is a prominent example of such a strategy. The CO2M concept relies on a constellation of sun-synchronous satellites with XCO_2 spectral-imagers to be deployed from 2025 by the European Commission and the European Space Agency (ESA). It will be based on passive radiance measurements in the
45 Short-Wave InfraRed (SWIR), a part of the spectrum that is sensitive to CO_2 and CH_4 concentrations throughout the troposphere including the boundary layer, like almost all the space missions that have been dedicated to GreenHouse Gas (GHG) monitoring so far (Crisp et al., 2018).

Much remains to be understood and to be developed in order to ensure that such a constellation informs about emissions with enough detail to be relevant for policy makers. In this context, Observing System Simulation Experiments (OSSEs) of
50 atmospheric inversions with synthetic images of XCO_2 data have been supporting the design of the space missions that will monitor the anthropogenic emissions (Buchwitz et al., 2013; Pillai et al., 2016; Broquet et al., 2018). So far, they have mainly focused on plume inversions for some large plants and cities. However, Wang et al. (2018) estimated that cities and plants emitting more than $10 \text{ MtC}\cdot\text{yr}^{-1}$ like Berlin (in the study by Pillai et al. (2016)) and Paris (in the study by Broquet et al. (2018)) represent less than $\sim 7\%$ of the global CO_2 emissions. Furthermore, the studied cases are generally quite isolated
55 from other large CO_2 sources, facilitating the distinction of their plumes in the XCO_2 images, while plumes from neighbor sources could overlap and hamper the attribution to each underlying emission source. Finally, the signature of emissions in spaceborne imagery does not consist only of clear plumes from cities, industrial clusters and point sources. Despite the large atmospheric signature of the natural fluxes, atmospheric inversions may have the potential to exploit other spatial variations in XCO_2 fields to quantify regional to national budgets of more diffuse sources or of all types of sources, even when the
60 overlapping of several plumes prevent from quantifying individual cities and point sources. Therefore, there is a need to extend the OSSEs to a representative range of sources with various emission budgets and spreads, and various distances to other major sources, and to a larger range of spatial scales.



We have developed a high-resolution inversion system for the monitoring of CO₂ anthropogenic emissions at spatial scales ranging from local intense point sources like industrial sites to regional and national scales. Furthermore, this system accounts for the uncertainty in the natural fluxes. Our current simulation domain covers most of Western Europe with an extensive ensemble of cities, plants and diffuse CO₂ emissions. We use an analytical inversion methodology, which is the most adapted approach to efficiently test an important number of observation scenarios (section 2.1.2.), a high-resolution atmospheric transport model (section 2.1.1) and a high spatial resolution distribution of the emissions derived from different inventory products developed by the Institut für Energiewirtschaft und Rationelle energieanwendung (IER) of the University of Stuttgart (section 2.2).

The analytical inversion system follows the traditional Bayesian formalism of the atmospheric inversion. Of direct relevance here, it derives uncertainty statistics of its “posterior” emission estimates for the controlled sources (plants, cities, countryside areas or whole regions) from: i) the assumed uncertainties in the budgets derived from “prior” emission inventories (built on statistics of the fossil fuel consumption, activity data and emission factors), ii) the spaceborne XCO₂ observation sampling and precision, and iii) its atmospheric transport model. The improvement of the knowledge on the emissions enabled by the satellite imagery is quantified here in terms of “uncertainty reduction”, i.e. of the relative difference between the prior and posterior uncertainties.

The inversion system solves for hourly budgets of the emissions from the different types of sources over the 6 hours before the satellite observation of the corresponding area. Broquet et al. (2018) showed indeed that, due to atmospheric diffusion, the atmospheric signatures of emissions from a mega-city like Paris which are detectable, with current measurement capability in satellite XCO₂ images, correspond approximately to the city emissions occurring within less than 6 hours before the satellite overpass. This duration should be even shorter for the range of sources analyzed in our study since most of them have lower emissions than Paris. The analysis of the results will primarily focus on the 6h-budgets of the emissions before the satellite observation. However, controlling the hourly budgets allows evaluating the capability to solve for the temporal profiles of the emissions. It also allows accounting for some level of independence of the uncertainties in the emissions from different hours, which limits the ability to cross and extrapolate information throughout the 6-hour windows. This point is critical for cities whose detectable atmospheric signatures are representative of emissions on durations shorter than 6-hours, and thus for which there is no direct constraint from the satellite observation on the first hours of such 6-hour windows.

The OSSEs presented in this study use a rather simple simulation of the XCO₂ observation sampling and errors from a single helio-synchronous satellite over the area of interest. The aim is indeed to provide a general understanding of the performance of the inversion system and of its potential to monitor anthropogenic emissions with spaceborne XCO₂ imagery rather than to evaluate a precise mission configuration with precise orbital parameters and instrumental specifications. Nevertheless, a large range of values for the precision (assumed to be homogeneous in the satellite field of view), horizontal resolution and swath of a spaceborne instrument are tested to assess the impact of these parameters on the inversion results, which can potentially support the design of future missions (section 3.2.).



Furthermore, in order to get a wide range of atmospheric transport conditions (in particular for wind speed, (Broquet et al., 2018)) and natural flux conditions (Pillai et al., 2016), inversions are performed for each day of March and May 2016. We work with full images of the plumes from the targeted sources each day, by flying a satellite any day in its vicinity with a large swath. Partial images of the plumes will be analyzed when studying the sensitivity to the swath width (over Paris) only.

100 The cloud cover and the corresponding gaps in the spaceborne passive XCO₂ sampling are ignored. In any case, the satellite crosses the area of interest at 11:00 (local time used hereafter) similar to what is currently recommended for the CO2M mission (Pinty et al., 2017), so that the inversion controls the hourly emissions of the sources between 5:00-11:00.

The inversion system and the corresponding transport model extend from South France to North Germany and from Western UK to Eastern Germany (Fig. 1). However, the grid of the transport is zoomed and the analysis focuses on a 2 km-resolution

105 sub-domain covering the North of France (in particular Paris), South East England (in particular London), West Germany, Belgium, Luxembourg and the Netherlands.

The first part of the analysis concerns the monitoring of the emissions of Paris and its suburb which represent the most populated and densest urban area of Europe. Broquet et al. (2018) chose this megacity as a study case because its emissions are high (~11-14 MtC·yr⁻¹ for 2013 according to the AIRPARIF inventory (Staufer et al., 2016; AIRPARIF 2013)),

110 concentrated and relatively distant from other major sources. The topography of the region is moreover relatively flat and the average wind speed is moderate: 7 m·s⁻¹ on average at 100 m above the ground level (Broquet et al., 2018). The XCO₂ plume generated by the Paris emissions has a relatively simple structure that often emerges well from the background. The monitoring of the emissions of Paris constitutes thus a very favorable case with respect to other cities in Europe. Broquet et al. (2018) performed some analysis of the sensitivities of the inversion results as a function of the wind speed and of the

115 XCO₂ spaceborne spectro-imagery average precision and horizontal resolution. However, they tested a limited number of values for these observation parameters, and in particular few high precisions (< 2 ppm) and a single high spatial resolution (< 4 km) value, while the refinement of the specification of new missions requires understanding of the sensitivity to choices of precision at the 0.1 ppm scale and of resolution at the 1 km² scale; these choices having large impacts on the design of the instrument and therefore on its cost (Pinty et al., 2017). Furthermore, Broquet et al. (2018) performed all their OSSEs with a

120 unique hypothesis on the prior uncertainties in the 1-hour to 6-hour budgets of the emissions from Paris, while acknowledging that this characterization could have a significant impact on the results and that the uncertainties in the inventories at such a temporal scale are difficult to assess. Therefore, this study performs a deeper investigation of the sensitivity to the observation precision and spatial resolution, to the wind speed and to the characterization of the uncertainties in the prior estimate of the emissions (section 3.2).

125 The second part of this study considers the full ensemble of emission sources from point sources to regions in the 2-km resolution sub-domain. This sub-domain encompasses the Netherlands, Belgium and West Germany which are characterized by densely populated areas distributed over a network of medium-sized towns and by a large number of strong point sources, with some power plants in West Germany emitting for example more than 5 MtC·yr⁻¹. The ability of the inversion system to disentangle the plumes of neighbor sources is therefore well challenged in these areas.



130 This paper is organized as follows: section 2 details the theoretical and practical framework of both the inversion
system and of the OSSEs conducted in this study. Section 3 analyses the results relative to the monitoring of the emissions of
Paris and in particular the corresponding sensitivity analyses (section 3.2). This section also diagnoses the potential of the
inversion system to monitor the anthropogenic emissions at the point source, city and regional scales in the area where flux
and concentrations are simulated at 2-km resolution (section 3.3). Section 4 addresses the robustness and extent of the
135 conclusions that can be derived from this study and proposes some perspectives regarding the analytical inversion system
and the monitoring of anthropogenic emissions based on satellite data.

2. Inverse modeling system and OSSEs

In the following sections, we describe the different structural elements of the analytical inversion system: the gridded
inventories used to define the point or area sources to be controlled, and to map their emissions (section 2.2), the simulation
140 of the atmospheric CO₂ and XCO₂ signatures of the controlled sources using the atmospheric transport model CHIMERE
and the matrix computation of the posterior uncertainties in the emissions (sections 2.1.1 and 2.3). We also describe the
observations and parameters chosen for the OSSEs in this study: the XCO₂ observation sampling and errors (section 2.1.2)
and the prior uncertainties in the emissions (section 2.4). These observations and parameters can be easily modified to
conduct new OSSEs with the analytical inversion system. However, for the sake of clarity, the descriptions of i) the
145 components of the inversion system and of ii) the options for the OSSEs are intertwined.

2.1. XCO₂: transport model simulations and pseudo-data

2.1.1. Simulations of CO₂ and XCO₂ with the CHIMERE model

To compute the 4D CO₂ signatures of surface CO₂ fluxes in the study domain and for March and May 2016, and of the
domain CO₂ boundary conditions, we use the regional atmospheric transport model CHIMERE (Menut et al., 2013). This
150 Eulerian mesoscale model was designed to simulate pollution (Pison et al., 2007) but has also been used for CO₂
atmospheric inversion, and in particular for city-scale inversions of the emissions from Paris (Bréon et al., 2015; Staufer et
al., 2015; Broquet et al., 2018). It has shown high skill in simulating the daily and synoptic variability of the atmospheric
CO₂ concentrations at European CO₂ continuous measurements sites (Patra et al., 2008).

The domain of our CHIMERE configuration covers most of Western Europe (Fig. 1) between latitudes ~42°N
155 (Northern Spain) and ~56°N (Northern Germany) and between longitudes 6°W (Eastern Ireland) and ~17°E (Eastern
Germany). The horizontal and vertical resolutions of the zoomed grid of this configuration range from 2 to 50 km; the 2 km
× 2 km resolution sub-domain being appropriate to simulate the atmospheric signature of a dense network of sources in
Northern France, Belgium, the Netherlands, Luxembourg and Western Germany. The zoom and the extent of the CHIMERE
grid together link the simulation of CO₂ at local scales in this area of interest with the transport of CO₂ at the European scale
160 while mitigating the computational cost. The model has 29 sigma vertical layers that extend from the surface to 300 hPa.



Model concentration outputs are averaged at the hourly scale. The meteorological forcing is from the 9 km × 9 km- and 3-hour- resolution analysis of the European Center for Medium-Range Weather Forecasts (ECMWF). The CO₂ concentrations used to impose the conditions at the initial time and at the lateral and top boundaries of the CHIMERE domain are from the analysis of the Copernicus Atmosphere Monitoring System (CAMS, (Inness et al., 2019)) at ~16 km resolution. The products used to impose surface CO₂ fluxes in the model are detailed below in section 2.2.

XCO₂ observations and the corresponding signatures of fluxes are simulated from the CO₂ 3D fields from CHIMERE at 11:00. For the sake of simplicity in the OSSEs conducted here, since only synthetic data are used, and since a rather simple modeling of the spaceborne observation is used, the computation of XCO₂ assumes that the vertical weighting function of the CO₂ column-averaging (kernel) is vertically uniform. For a given model pixel at latitude *lat* and longitude *lon*, XCO₂ is thus computed from the vertical average of the CO₂ mole fractions simulated by the model:

$$XCO_2(lat, lon) = \frac{\int_{P_{top}}^{P_{surf}} CO_2(lat, lon, P) dP + \overline{CO_2}(P_{top}) P_{top}}{P_{surf}(lat, lon)}, \quad (1)$$

where *P* designates the atmospheric pressure, *P_{surf}* the atmospheric surface pressure and *P_{top}* (300hPa) the pressure ceiling of the model. For pressures lower than *P_{top}*, we assume that the CO₂ concentrations equal the horizontally-average top-level mixing ratios in CHIMERE ($\overline{CO_2}(P_{top})$). Indeed, we do not expect significant spatial gradients of CO₂ over the simulation domain in the upper atmosphere.

2.1.2. XCO₂ pseudo-data sampling and error

As detailed in section 2.3 below, the OSSE framework of the inversions requires the location and time of the individual XCO₂ data, and the associated error statistics, but not the explicit values of the synthetic observations themselves. In this study, we consider pseudo satellites with a Low Earth Orbit (LEO) whose altitude and inclination parameters are similar to the ones of the A-Train (98.2° and 705 km respectively, (Parkinson et al., 2006)). The satellite observations are assumed to happen at 11:00 in the morning. Successive tracks for a single satellite on this orbit are distant by about 25 degrees. However, we do not study the potential of a specific satellite nor that of a constellation of such LEO satellites depending on of their number. This study focuses on statistics of the imagery at the scale of 6-hours. Therefore, it will consider single satellite tracks for any day that do not correspond to a specific positioning of a satellite on the chosen orbit: when studying the emissions of the Paris urban area, it follows the track which crosses this city every day and various swaths are considered to study the sensitivity of the results to this parameter (section 3.2). For the study of the multiple sources contained within the 2-km sub-domain (section 3.3), it follows a track centered over Belgium and we use a 900-km swath to ensure a full coverage of the plumes from these sources (the sensitivity to a realistic range of swath widths is not investigated in this second set of analysis).

Our OSSEs assess the impact on the inversion results of the measurement noise of the satellite instrument only, ignoring the errors associated to the radiative transfer inverse modeling for the retrieval of the XCO₂ data from the radiance



measurements (Buchwitz et al., 2013; Broquet et al., 2018), and in particular any “systematic error”. The errors on the XCO₂ data at the spatial resolution of the measurements are thus assumed to be Gaussian, unbiased and uncorrelated in space or time. The distribution of the standard deviation (STD) for these errors is also assumed to be uniform and these errors are therefore summarized by a single value of STD (denoted the data precision hereafter).
195

A large number of scenarios are tested for the observation specifications: the precision on the individual XCO₂ data varies between 0.3 and 2 ppm, and the spatial resolution of the ground pixels can take the following values: 2 km×2 km (longitude × latitude), 2 km×3 km, 3 km×3 km, 3 km×4 km and 4 km×4 km. The reference is a precision of 0.6 ppm and a spatial resolution of 2×2 km². These values are similar to the characteristics of the simulated CO₂M data used in the study of Wang et al. (2020). When studying the sensitivity of the results over Paris, to the swath of the instrument varies from 100 km to 600 km, with a reference value of 300 km.
200

2.2. CO₂ fluxes

2.2.1. Maps and time-series of anthropogenic emissions and natural fluxes

High resolution maps of anthropogenic emissions are needed to define appropriate point and areas sources to be controlled by the inversion. High resolution maps of anthropogenic and biogenic fluxes are also needed to distribute the controlled local to regional budgets of these fluxes over the spatial grid of the CHIMERE model. Finally, such maps are needed to provide insights on the typical budgets of fluxes at the control resolution, and thus to quantify the prior uncertainty in these budgets with a suitable order of magnitude.
205

The anthropogenic CO₂ emissions are extracted from several datasets compiled by IER (Pregger et al., 2007; Thiruchittampalam et al., 2012). These datasets provide maps of the annual budgets per sectors of anthropogenic activities over different domains, and at different spatial resolutions. We have merged and re-gridded them to derive a map of the annual budgets over the entire grid of the CHIMERE configuration. The emissions corresponding to France and Germany are extracted from the respective IER national maps for 2005 at a 1-minute resolution while emissions in Belgium, Luxembourg and the Netherlands are derived from an IER 1-km product covering Northern Europe for 2005; the IER 5-km resolution map covering the whole Europe for 2008 is used for the emissions over the rest of the domain. The gridded spread sources in these maps are interpolated on the CHIMERE grid but the large point sources are relocated as point sources in individual CHIMERE grid cells. We then derive the hourly emission maps from the yearly emission maps by applying the convolution of IER typical temporal profiles specific to each country and sector. These profiles include seasonal, daily and diurnal variations of emissions for large sectors such as traffic, power demand, domestic heating or air conditioning (Pregger et al. 2007).
210
220

The IER maps for France, Germany, Northern Europe and the whole Europe correspond to annual budgets for years (2005 and 2008) that can be different from one area to the other, and which are different from the year chosen for the atmospheric transport and for the natural fluxes (2016). This could raise some inconsistencies if assimilating real data in the inversion.



225 However, this study is based on OSSEs with some strong simplifications regarding the observation system since the overarching target is a general understanding of the behavior and potential of the inversion. This requires the use of a high resolution and realistic distribution of the emissions in space and time, but not a precise estimate of their amplitudes for a given year.

230 The land surface natural fluxes are derived from 8-km resolution simulations made with the Vegetation Photosynthesis and Respiration Model (VPRM) model for the year 2016. This prognostic model delivers hourly values of Net Ecosystem Exchange (NEE) by assimilating satellite and meteorological data (Mahadevan et al., 2008). These are interpolated over the CHIMERE area at the hourly time scale. Natural ocean fluxes are ignored.

2.2.2. Controlled areas

235 The resulting hourly maps of anthropogenic CO₂ emissions for spread sources and large point sources are decomposed spatially to define the areas for which hourly emission budgets are controlled by the inversion: large point sources, cities, remaining part of regions where point sources and cities have been extracted (covering diffuse emissions only), and full regions when point sources and cities are not controlled separately but altogether with the diffuse emissions. Hourly budgets of the natural fluxes are controlled for full regions only, the regions used for the control of anthropogenic and biogenic fluxes being identical.

240 The definition of the regions is done considering the whole domain. It corresponds to administrative regions of France, Belgium, the Netherlands, Luxembourg and Germany, and to three additional large “regions”: the United Kingdom, Switzerland and the rest of the domain. This subdivision results in 67 regions (Fig.1). These 67 regions correspond to the spatial resolution of the natural fluxes in the inversion.

245 Point sources and cities are controlled individually in the 2-km resolution part of the CHIMERE grid only (section 2.1.1., Fig. 1). In the 39 regions entirely comprised within this sub-domain, we individually control the 84 point sources (e.g., factories, power plants...) whose annual emissions are larger than 0.2 MtonC.yr⁻¹. The maps of the remaining emissions (excluding these point sources) in each of these 39 regions are then processed to extract large urban areas to be controlled independently, ensuring at least one controlled urban area per region, and that no control urban area overlaps two different regions. An algorithm of pattern recognition has been designed for such an extraction, with the idea that urban areas correspond to clusters of adjacent high emitting pixels (also followed by (Wang et al., 2018)). After having applied a
250 Gaussian filter to smooth the spatial distribution of emissions, the large urban areas are defined by a label-connecting algorithm (Shapiro et al., 2000) which defines the clusters of adjacent points whose emissions are above a predefined threshold. As the density and extension of cities considerably vary amongst the different regions, the parameters of the pattern recognition algorithm, i.e. the standard deviation of the Gaussian filtering and the emission threshold, are different for each region to ensure that each region contains at least one controlled urban area (Fig. 2). As a result, we identify
255 control urban areas within the 2-km resolution sub-domain. They are characterized by a wide range of budgets and spread of their emissions, the annual budgets ranging between ~0.07 MtonC.yr⁻¹ and ~9.9 MtonC.yr⁻¹ (with a mean and a standard



deviation of $\sim 0.8 \text{ MtonC.yr}^{-1}$ and $\sim 1.5 \text{ MtonC.yr}^{-1}$ respectively), and areas ranging from $\sim 8 \text{ km}^2$ to $\sim 2400 \text{ km}^2$ (with a median value of $\sim 240 \text{ km}^2$).

260 The remaining emissions, after having extracted the large point sources and urban areas in the 39 regions, are considered to be diffuse and called hereafter the “countryside” emissions. The inversion controls their budgets in each region. The analysis of the results at the regional scale for these 39 regions will consider either the countryside emissions only (i.e. focusing on the individual control variables), or their aggregation with the emissions from the point sources and cities within the same region (i.e. considering the full geographical extent of the regions). The inversion also directly controls the total budget of the emissions for the 28 regions that are not fully comprised in the 2-km sub-domain (most of these 28 regions do not
265 actually overlap this sub-domain at all). Overall, the control of countryside or total regional emissions adds 67 areas (corresponding to the 67 regions) for the anthropogenic emissions so that the inversion controls the hourly budgets of anthropogenic emissions for 303 areas (84 point sources, 152 urban areas and 67 countryside areas) and the hourly budgets of natural fluxes for 67 areas.

2.3. Analytical flux inversion

270 2.3.1 Theoretical framework

The inversion system follows a traditional analytical inversion approach based on the Bayesian formalism and assuming Gaussian errors statistics (Tarantola et al., 1987; Broquet et al., 2018). The system controls factors that scale the hourly budgets of the different control areas for the anthropogenic and biogenic fluxes defined in section 2.2.3. It also controls a single scaling factor applied to the CO_2 field used to impose the initial, lateral and top boundary CO_2 conditions (BC) of the
275 model, since such boundary conditions generally bear important large-scale uncertainties that can impact the estimates of sources within the domain (Broquet et al., 2018). In the OSSEs of this study, more specifically for each day in March or May 2016, the inversion periods cover the 6 hours (5:00-11:00) before 11:00 when the satellite observations are supposed to be made. The number of control variables ($2221 = 370 \text{ controlled areas} \times 6 \text{ time slots} + 1 \text{ control variable for the BC}$), is sufficiently small for analytical calculations to solve the inverse problem. However, building the matrix which encompasses
280 the atmospheric transport operator \mathbf{H} described below (section 2.3.2) requires a large computational burden.

For a given inversion period, we define the control vector \mathbf{x} as the set of controlled scaling factors for the hourly emission budgets and the boundary conditions. The prior uncertainty in \mathbf{x} is assumed to be Gaussian and unbiased and is thus characterized by the uncertainty covariance matrix \mathbf{B} .

In this study, the observation vector \mathbf{y} is defined by the XCO_2 concentrations in the transport model horizontal grid cells
285 sampled by the observations. The simulation of \mathbf{y} based on a given estimate of \mathbf{x} is given by the linear observation operator \mathbf{H} : $\mathbf{x} \rightarrow \mathbf{y} = \mathbf{H}\mathbf{x}$, which chains three operators. The first operator $\mathbf{H}_{\text{distr}}$ distributes the controlled hourly budgets of emissions in space within the controlled areas, and provides the spatial and temporal mapping of the boundary conditions whose scaling factor is controlled by the inversion. The second operator $\mathbf{H}_{\text{transp}}$ is the atmospheric transport from the emissions and the



boundary conditions to the full CO₂ and XCO₂ fields. Finally, the third operator $\mathbf{H}_{\text{sample}}$ performs the XCO₂ sampling at the
290 location of the XCO₂ data (section 2.1.1). Differences between $\mathbf{H}\mathbf{x}$ and observed values for \mathbf{y} arise due, on the one hand, to
uncertainties in \mathbf{x} , and, on the other hand, to the combination of errors in the observation operator and in the observation data
that are altogether called “observation errors”. The errors from the observation operator are strongly associated with the
atmospheric transport model error (Houweling et al., 2010; Chevallier et al., 2010), but also with the discretization and
spatial resolution of the transport and inversion problems, which raise representation and aggregation errors (Kaminski et al.,
295 2001; Bocquet et al., 2011). Assuming that they are Gaussian and unbiased like the prior uncertainties, these observation
errors are fully characterized by the observation error covariance matrix \mathbf{R} . The \mathbf{H} , \mathbf{B} and \mathbf{R} matrices must be explicitly
estimated in the analytical inversion framework (section 2.3.2 and 2.4).

The Bayesian theory (Tarantola et al., 1987) states that the statistics of the knowledge on \mathbf{x} knowing i) the prior estimate of
 \mathbf{x} , ii) the observed values for \mathbf{y} and iii) \mathbf{H} as a link between the \mathbf{x} and \mathbf{y} spaces, follow a Gaussian and unbiased distribution.
300 The uncertainty in such a posterior estimate is thus fully characterized by the posterior uncertainty covariance matrix \mathbf{A}
given by:

$$\mathbf{A} = [\mathbf{B}^{-1} + \mathbf{H}^T \mathbf{R}^{-1} \mathbf{H}]^{-1} \quad (2)$$

The analysis of \mathbf{A} and its comparison to \mathbf{B} , aggregated or not over different spatial and temporal scales, are the critical
diagnostics in this study to assess the potential of inversions assimilating XO₂ images. The score of uncertainty reduction for
305 a given flux budget is a common indicator for evaluating the performance of an observation system. It is defined as the
relative difference between the STD of the prior (σ_{prior}) and posterior (σ_{post}) uncertainties in this flux budget ($UR = 100 \times$
 $(1 - \frac{\sigma_{\text{post}}}{\sigma_{\text{prior}}})$). If the assimilation of satellite observations perfectly constrains a given flux budget, the corresponding UR
equals 100%. If this assimilation does not provide any information on the flux budget, UR equals 0%.

2.3.2. Building the observation operator matrix \mathbf{H}

310 The analytical inversion system is essentially built on the explicit computation of $\mathbf{H} = \mathbf{H}_{\text{distr}} \mathbf{H}_{\text{transp}} \mathbf{H}_{\text{sample}}$. The different
columns of \mathbf{H} correspond to the signatures (or “response functions”) in the observation space of the different control
variables, *i.e.* of the different hourly emissions for each control area, and of the boundary conditions. They are computed by
applying the sequence of operators $\mathbf{H}_{\text{distr}}$, $\mathbf{H}_{\text{transp}}$ and then $\mathbf{H}_{\text{sample}}$ to each control variable set to 1, keeping the others null
(Broquet et al., 2018). $\mathbf{H}_{\text{distr}}$ is defined based on the flux maps detailed in sections 2.2.1. and 2.2.2. $\mathbf{H}_{\text{transp}}$ corresponds to the
315 CHIMERE model and to the vertical integration of CO₂ into XCO₂ presented in section 2.1.1, while $\mathbf{H}_{\text{sample}}$ corresponds to
the sampling, on the transport model grid, of the simulated XCO₂ values according to the spatial distribution of the pseudo-
observations (section 2.1.2). A generalized \mathbf{H} is actually stored for the analytical inversion system to anticipate any option
for $\mathbf{H}_{\text{sample}}$, by recording the full CO₂ and XCO₂ fields from the application of $\mathbf{H}_{\text{distr}} \mathbf{H}_{\text{transp}}$ to each control variable, *i.e.* the full
CO₂ and XCO₂ signatures of each control variable.



320 2.4. Practical implementation of the OSSEs

While, in principle, \mathbf{R} should characterize both the XCO_2 data errors and the errors from the observation operator \mathbf{H} , this study focuses only on the impact of the observation sampling and errors. It ignores the errors from the observation operator. Moreover, the observation errors are restricted to the measurement noise which is uncorrelated in space and time as detailed in section 2.1.2. The different \mathbf{R} matrices used for the OSSEs (depending on the observation sampling and noise) are thus all
325 diagonal. The errors on the individual pseudo-observations are described by a uniform precision (σ_{XCO_2}) depending on the chosen satellite configuration (section 2.1.2). However, the observation vector \mathbf{y} is defined by the transport model grid rather than by the precise location and coverage of the data. The diagonal elements of \mathbf{R} follow thus the aggregation of n_{obs} pseudo observations with uncorrelated errors (where n_{obs} is potentially greater than 1) within each model grid cell corresponding to an element of \mathbf{y} , so that the resulting STD of the errors for this element is given by $\frac{\sigma_{XCO_2}}{\sqrt{n_{obs}}}$

330 Prior estimates of anthropogenic emissions and biogenic fluxes are generally provided by inventories and ecosystem model simulations such as those used here in \mathbf{H}_{distr} to distribute the fluxes at high resolution. \mathbf{B} should characterize uncertainties in such products and is thus be set with values corresponding to typical relative uncertainties in the budgets from the maps detailed in section 2.2.1. When constructing the \mathbf{B} matrices in all our OSSEs, we assume that there is no correlation between the prior uncertainties associated to different controlled emission areas or between these uncertainties and the one associated
335 to the boundary conditions. However, we model the temporal correlations between prior uncertainties in scaling factors associated to different hourly natural or anthropogenic flux budgets of the same controlled emission area by using an exponentially decaying function with a correlation time scale τ (like, for instance, in (Bréon et al., 2015)):

$$\rho_{i,j} = e^{-\frac{|j-i|}{\tau}} \quad (3)$$

where j and i are the indices of two corresponding hours. The STD of the prior uncertainties in the scaling factors for the
340 different hourly budgets of the same controlled area are fixed to an identical value σ_{hour} . Finally, we assume that the STD of the prior uncertainties in scaling factors for the 6-hour budgets of the natural fluxes or anthropogenic emissions from a controlled area during 5:00-11:00 (to be applied to the budgets from the IER and VPRM products presented in section 2.2.1 and used to build \mathbf{H}_{distr}) is fixed to a value σ_{Budget} that is the same for all control areas: typically 50% or 100% of the 6-hour budgets. The STD of the prior uncertainties in the scaling factors for the hourly budgets of the controlled areas σ_{hour} are then
345 derived based on these different assumptions. The reference parameters for \mathbf{B} are fixed to $\tau = 3$ hours and $\sigma_{Budget} = 50\%$. Despite the differences between the temporal variations of the hourly emissions from one control area to the other in \mathbf{H}_{distr} , these STD show a negligible variation of less than 1% and when considering this reference set-up for \mathbf{B} , $\sigma_{hour} \sim 65\%$. The sensitivity of the inversion to the values of σ_{Budget} and τ is assessed in section 3.2.3.



3. Results

350 3.1. High-resolution simulations of XCO₂

Previous sections documented how, for each 6-hour period, the inversion system exploits the simulated XCO₂ fields at 11:00 to constrain each hourly budget of the anthropogenic or natural fluxes of the controlled areas between 5:00 and 11:00. The CHIMERE full XCO₂ simulations between 5:00 and 11:00 with the anthropogenic emissions, natural fluxes and/or domain boundary conditions detailed in sections 2.1 and 2.2 are used in this section to compare the overall signature of these components and of the controlled areas, and to discuss their overlapping. Figure 2b shows the XCO₂ signatures of all the anthropogenic emissions in the domain excepted those from the 84 point sources controlled individually by the inversion in the 2-km resolution subdomain (that are illustrated in Fig. 2a). Figure 2.c integrates the XCO₂ produced by the 84 point sources and shows the signature of all the anthropogenic emissions. Finally, figure 2d. displays the superposition of the XCO₂ signatures of all the anthropogenic emissions, natural fluxes and of the boundary conditions. For all these figures, XCO₂ values are taken at 11:00 and are provided by simulations between 5:00 and 11:00 on May 23rd which is a day of strong northwest-southeast wind ($\sim 10 \text{ m}\cdot\text{s}^{-1}$ over Paris at 700 m above ground level).

The strong plumes from the megacities of Paris and London are easily distinguished when considering the signature of anthropogenic emissions in Fig. 2b and 2c, with their amplitude exceeding 0.3 ppm at 100 km downwind of these cities, and with sharp gradients of XCO₂ at their edges. The relative narrowness, extended length and small intensity of the plumes shown in the Figs. 2b and 2c are explained by the magnitude of the wind speed on May the 23rd ($\sim 9 \text{ m}\cdot\text{s}^{-1}$ over Paris). The characteristics of those plumes vary considerably with respect to the wind speed and the inversion results are strongly impacted by this parameter (section 3.2.1 and Broquet et al. (2018)).

Figures 2b and 2c also show that the overlapping of plumes from urban areas of Belgium and the Netherlands produces XCO₂ patterns whose amplitudes are comparable to that of the plumes from Paris and London. Due to the urban density of those countries, the level of distinction of the individual signatures of the different cities is however weak. If we exclude Paris, Northwestern France has a much less dense urban fabric with scattered cities of small extensions. Thus, this sparse distribution allows the relatively weak plumes of cities emissions to be visible, whereas the more diffuse XCO₂ signatures of the anthropogenic emissions of the countryside do not form any distinguishable patterns (Fig. 2b).

The comparison between Figs. 2b and 2c highlights the plumes from some of the large 84 point sources within the 2-km resolution subdomain (section 2.2.3). The amplitude of these plumes can locally reach that of Paris but such an increase above the background occurs on a much smaller extent: the one of the power plant close to Dunkerque ($\sim 51^\circ$, $\sim 2.3^\circ$) in the Northern French coast reaches 0.4 ppm but its width does not extend to more than 5 km for instance (Fig. 2c). The capacity of our high resolution transport model to simulate narrow XCO₂ plumes from point sources or urban areas distinct from neighbor or surrounding sources is revealed by the example of several point sources in Belgium as well as that of the oil refinery of Grandpuits (48.59° , 2.94°) whose plume stands out of the large plume from the Paris urban area (Fig. 2c). The 2-



km resolution zoom of the model grid allows distinguishing those features which would otherwise be blurred in a coarser resolution transport model.

When including the XCO_2 produced by the natural fluxes and the boundary conditions, identifying the features produced by the anthropogenic emissions is more difficult (Fig. 2d). The atmospheric signatures of Paris, of London and of the high-emitting power plants are hardly differentiated from patterns produced by the boundary conditions and natural fluxes even though they are still visible. The scattered cities with small extensions and low emission budgets which produce isolated plumes of low amplitudes can hardly be seen. The boundary conditions and the natural fluxes tend indeed to produce signatures whose amplitude is often larger than the anthropogenic emissions, or at least comparable, which interfere with and blur the signals of these emissions, specially with those of the diffuse anthropogenic emissions. Boundary conditions and natural fluxes are however much more homogeneously distributed than the anthropogenic emissions, that are localized over a small fraction of the surface. As a consequence, the boundary conditions and the natural fluxes produce smooth XCO_2 fields (Fig. 2d) while the anthropogenic emissions from sources inside the domain produce heterogeneous fields with smaller and finer structures and sharper gradients (Fig. 2c). Therefore, the separation between the two types of fluxes could rely on the differences in terms of spatial scales of their spatial signatures, or on a precise knowledge of the atmospheric transport patterns.

This first qualitative overview of the atmospheric signatures could imply that the ability to quantify the budgets of emissions from the two megacities, from most of the 84 large point sources, and for large regions in the North East should be much larger than for the individual urban areas in most of the domain or for the countryside emissions. However, this diagnostic test relies on a qualitative assesment of Figures 2*i*. In Section 3.3, we will quantitatively analyze the implications for the inversion results of the differences in terms of amplitude or spatial structure between the XCO_2 signatures.

3.2. Potential of the satellite images to monitor the anthropogenic emissions of a megacity: sensitivity studies

This section assesses the performance of our inversion assimilating XCO_2 images to monitor the anthropogenic emissions from the Paris area, as a function of the wind conditions for speed and direction, of the XCO_2 observation precision, resolution and swath, and of the configuration of the prior error covariance matrix **B**. Results are relative to the inversion control area that covers most of the Paris urban area (Fig 2.a.) and whose contours have been delimited by the pattern recognition algorithm described in section 2.2.3. The analysis is based on 62 6-hour inversion tests with satellite images centered on this area for each day of March and May 2016. With the reference 300-km wide swath, such images cover the plumes from the Paris urban area entirely for most wind conditions [Broquet et al. 2018]. In the following, the wind speed is characterized by its averaged value at 700 m above ground level over the inversion control area corresponding to Paris and over the period corresponding to the diagnostic test: over 5:00-11:00 when analyzing the uncertainty in the budgets of the emissions corresponding to the full 6h-period of inversion, or over the time interval [hh,11:00] when analyzing the uncertainty in the hourly budget of the emissions between the hours hh and 11:00h.



3.2.1. Impact of the wind speed

A first set of inversions is conducted with the reference values for the precision, resolution and swath of the satellite
415 observation and for the parameters of the prior uncertainty. These inversions are applied to 12 different days in March 2016
which present a range of average wind speeds from 2 to 14 $\text{m}\cdot\text{s}^{-1}$ (Fig. 3). We investigate results in winter, when the
amplitudes of the biogenic fluxes are low, to mitigate the influence of these fluxes, and of their variability, on the URs of the
Paris emissions. Note that the time profiles modeling the variability of the anthropogenic emissions ignore day-to-day
420 variations (except between week-end and working days) which almost removes the influence of the variability of these
emissions when studying only the month of March. Results are presented in terms of prior and posterior uncertainties in both
the 1-hour and 6-hour budgets of emissions from the Paris urban area. The directions of the wind are predominantly
meridional so that the selection of the swath has no impact. The main analysis and conclusions in this section are similar to
that of Broquet et al. (2018) and we thus present them briefly.

Results in Fig. 3 illustrate the fact that larger wind speeds lead to smaller uncertainty reductions for the 6 h-emission
425 budgets: On March 3 when the average wind speed is $13.5 \text{ m}\cdot\text{s}^{-1}$, the UR for the reference values for the precision,
resolution and swath is 74% while on March 10 (average wind speed $\sim 1.8 \text{ m}\cdot\text{s}^{-1}$) the UR is of 97% (Fig. 3a). Stronger winds decrease
the UR because, due to an increased atmospheric dilution, the amplitude of the city plume is smaller which decreases the
signal-to-noise ratio for the inversion. However, when considering the UR for hourly emissions, this rule may not apply for
wind speeds lower than $6 \text{ m}\cdot\text{s}^{-1}$. For this range of wind speeds, the posterior uncertainty in individual 9:00-10:00 and 10:00-
430 11:00 emissions increases with decreasing wind speed (Fig. 3b). The inversion system shows difficulties in distinguishing
the atmospheric signatures produced by consecutive hourly emissions because these signatures have a significant overlap
when the wind speed is low. This explanation is confirmed by the negative correlations found between the uncertainties in
consecutive hourly emissions since the magnitude of these negative correlations increases when the wind speed decreases
(Fig. 3c). Important negative correlations explain also that for low wind conditions, 6h-emission budgets are better
435 constrained even though hourly emissions can be poorly constrained. The overestimation of some hourly emissions is
compensated by the underestimation of other hourly emissions.

The uncertainty reductions for 1h- and 6h-budgets are important for a large range of wind values: for the range considered in
this study, the UR for the 6h-budgets are above 74% and the UR for the 1h-budgets after 7:00 are above 62% (Fig. 3a).
Concerning the 1h-budgets of the 5:00 to 7:00 emissions, the corresponding UR significantly decrease for wind speeds above
440 $10 \text{ m}\cdot\text{s}^{-1}$. The UR for the 5:00 to 6:00 emission drops below 20%. This behavior is consistent with the fact that the signatures
of emissions occurring well before the satellite overpass have been much more diffused through atmospheric transport at the
observation time than that of later emissions.



3.2.2. Impact of the precision, resolution and swath of the satellite images

Figures 4a-d show the uncertainty reductions for the 6 h-emission budgets of March 3 (with a strong wind), March 10 (with a
445 low wind), May 23 (with a strong wind) and May 27 (with a low wind). This figure is associated to the first analysis made in
this section and corresponds to a second set of inversions performed with the range of options for satellite data precisions
and resolutions presented in section 2.1.2 but with the swath of the satellite track, the relative prior uncertainty in the 6 h-
budgets and the correlation length scale for the prior uncertainties in hourly fluxes fixed to the reference values (respectively
300 km, 50% and 3 hours). The sensitivity of the UR to the measurement precision and resolution increases with stronger
450 winds. For example, on May 27 ("weak" wind) and 23 ("strong" wind), the UR increases by 16% and 48% respectively
between inversions with 2 ppm precision data and inversions with 0.3 ppm precision data (at the resolution of $2 \text{ km} \times 2 \text{ km}$).
For those two days, the UR decreases by 6% and 20% respectively between inversions with $2 \text{ km} \times 2 \text{ km}$ resolution data and
inversions with $4 \text{ km} \times 4 \text{ km}$ resolution data (for a precision of 0.6 ppm). The comparison between results on March 3 and
10 confirms such a high sensitivity for stronger winds. It is related to the fact that the slope of the convergence of the UR
455 towards 100% with better precision and finer resolution is smaller with low wind speed, which generate higher UR than high
wind speeds. For similar reasons, the sensitivity to the precision decreases at finer resolution, and the sensitivity to the
resolution decreases with better precision (Figs. 4a-d).

The comparison between results obtained when doubling the random measurement error of the individual observations and
when multiplying by four the value of their spatial resolution provides insight into the exploitation of the fine scale patterns
460 of the XCO_2 image by the inversion. Indeed, both changes result in doubling the resulting error at coarse resolution, but
doubling the random measurement error at fine resolution conserves the capability to exploit information at this fine
resolution unlike coarsening the spatial resolution of the image. Figs. 4a-d show that scores of UR with $2 \text{ km} \times 2 \text{ km}$
resolution and 2 ppm precision data are extremely close to that with $4 \text{ km} \times 4 \text{ km}$ resolution and 1 ppm precision data. UR
with $2 \text{ km} \times 2 \text{ km}$ resolution and 1.2, 1, 0.8 or 0.6 ppm precision data are also similar to UR with $4 \text{ km} \times 4 \text{ km}$ resolution and
465 respectively 0.6, 0.5, 0.4 or 0.3 ppm precision data. This indicates that the inversions here do not really take advantage of the
information on the fine scale patterns of the plume from Paris.

A third set of inversions is conducted to study the sensitivity of the results to varying the width of the satellite swath keeping
all other observation and inversion parameters to reference values. This sensitivity is modulated by the wind conditions: the
speed and direction of the wind control the spread and position of the plume and thus the value of the swath which fully
470 covers the extent over which the amplitude of the plume is significant for the inversion, i.e., the value of the swath above
which the results do not change any more (Figs. 4e-h). This threshold value of the swath is lower for smaller wind speed. For
wind directions across the satellite track, the UR for the 6 h-emissions of the Paris area are no longer sensitive to the increase
of the swath above a value of 100 km and 400 km for wind speeds superior to $8 \text{ m}\cdot\text{s}^{-1}$ and to $9 \text{ m}\cdot\text{s}^{-1}$ respectively. The
sensitivity to the swath is null (except if considering very low values for the swath of the order of the width of the plume
475 from Paris) for wind directions along the satellite track, since considering satellite tracks centered on Paris.



3.2.3. Impact of the definition of the prior uncertainties on the CO₂ fluxes

The prior uncertainty covariance matrix \mathbf{B} has a strong influence on the scores of posterior uncertainties when its “amplitude” is comparable to, or much larger than, the one of the $\mathbf{H}^T\mathbf{R}\mathbf{H}$ matrix (see Eq. 2), i.e. once the prior uncertainties are comparable or much larger than the projection of the observation errors in the control space. The relative prior
480 uncertainties in the 6 h-emission budgets (σ_{Budget} , section 2.4.), which characterize the diagonal of \mathbf{B} , is one of the critical drivers of the relative weight given by the inversion to the prior information and to the observations.

In a fourth set of inversions, we thus analyze the sensitivity of the inversion results for 6-hour emission budgets to σ_{Budget} , with values for this parameter ranging between 0 and 100%. This set of inversions uses the reference values of the observation parameters and for the temporal autocorrelation of the prior uncertainties. Figs. 5a-b shows the corresponding
485 results on March 3 (with strong wind) and on March 10 (with low wind), to highlight the dependence of this sensitivity to the wind speed. The curves of UR as a function of σ_{Budget} have an inflection point for values around 50%. For low values of σ_{Budget} , the UR is sensitive to this parameter, the posterior uncertainty balancing the prior uncertainty and the projection of the observation error. For large values, the UR converges asymptotically towards 100%, and the posterior uncertainties are dominated by the projection of the observation error (i.e. the posterior estimate of the emission essentially rely on the top-
490 down information from the observation). The observational constraint on the inversion is larger on March 10 than on March 3 since the wind is much lower on the former. As a consequence, the qualitative threshold of σ_{Budget} above which the URs are not much sensitive to this quantity is smaller on March 10 than on March 3: 30% and 50% respectively.

These results over Paris suggests an empirical choice of a reference value for $\sigma_{\text{Budget}} \geq 50\%$, in the absence of any factual knowledge about σ_{Budget} . With 50% as a reference value, we focus our analysis of the posterior uncertainties on such a
495 projection of the information from the observation and we nearly neglect the prior information, while keeping an assumption regarding the prior uncertainties that could seem consistent or even optimistic compared to series of assessment of the errors in inventories for cities at daily scale (Wang et al., 2020). However, for other cities, point or area sources with smaller amplitudes, the observational constraint is lower. The relative weight between the projection of the observations and the prior information is then more balanced than for Paris, and the prior uncertainty still has a significant impact on the posterior
500 uncertainties when using $\sigma_{\text{Budget}} = 50\%$. In order to study the pure projection of the observation errors, results using $\sigma_{\text{Budget}} = 100\%$ will thus be analyzed along with that using $\sigma_{\text{Budget}} = 50\%$ in section 3.3.

The other important parameter defining the \mathbf{B} matrix in this study is τ (section 2.4.). By construction, the increase of the corresponding auto-correlations for the prior uncertainties at the hourly scale in \mathbf{B} does not modify the prior uncertainties of the 6 h emission budgets. However, it could help the inversion crossing the information on different hourly budgets to better
505 constrain the overall budget of emissions. A fifth set of inversions with the reference values for the observation parameters and for σ_{Budget} is conducted to test the sensitivity to τ , with values for this parameter from 0 to 6 hours (0 h indicating that there is no temporal correlation in \mathbf{B} , and 3 h being the reference value), on March 10 and 3. The analysis shows that, actually, the increase of τ hardly impacts the results for the 6 h-budgets (not shown) but significantly changes the results for



the hourly budgets (Figs. 5c-d). The auto-correlation brings information about the temporal distribution of the emissions, 510 constraining how the 6 h emission budgets are distributed at the hourly scale. This impact is more significant when the XCO₂ signatures of the hourly emissions overlap, i.e. for hourly emissions between 5:00-7:00 when the wind is high and for almost all the hourly emissions when the wind is low. But, this better knowledge about the temporal variations from auto-correlations does not appear to improve the knowledge on the 6 h-budgets.

3.3. Potential of satellite images to monitor anthropogenic emissions at the regional, city and local scales.

515 This section synthesizes the inversion results from the local scale (power plants, industrial facilities) to the regional scale over most of the 2-km resolution model subdomain, using a sixth set of inversions assimilating images that cover this subdomain entirely (satellite observations with a 900-km swath centered on Belgium, Fig.1). This set of inversions covers all the days of March and May 2016 in order to analyze the impact of the wind speed and of the natural fluxes on the results. The prior relative uncertainty in the 6-hour budgets of the emissions are alternatively set to $\sigma_{\text{Budget}}=50\%$ and 100%. These 520 inversions use the reference parameters for the observation precision and resolution and for the temporal auto-correlation of the prior uncertainties in hourly emissions (0.6 ppm, 2 km × 2 km and 3 hours respectively). Results over most of the 2-km resolution model subdomain using different observation spatial resolution and precision will briefly be discussed in section 4.

3.3.1. Overview of the inversion performance

525 Figure 6 gives a geographical overview of the score of UR in the 2-km resolution sub-domain. The largest scores of UR for 6-hour budgets are obtained for the mega-cities of Paris and London with a mean value >80% over the two months considered. Mean UR can also be >60% for several cities of Belgium and the Netherlands and for a large number of point sources (power plants and large industrial facilities) within the dense industrial area of western Germany, although these sources are close to each other or to other significant point and area sources.

530 In a general way, the scores of UR increase with the magnitude of the emissions (Fig. 7). This increase is more important when considering lower emission values due to the asymptotic convergence of the UR towards 100% for high emission values (with a point of inflexion for emitting sources of around ~2 MtC·yr⁻¹ in the curves of Fig. 7). The increase of the UR as a function of the budgets of emissions is different if considering point or area sources. As expected, the largest UR are obtained for narrower sources like point sources (Fig. 7a) and the cities (Fig. 7b) which generate plumes with smaller extents 535 but larger amplitudes than diffuse countryside emissions. When using $\sigma_{\text{Budget}} = 100\%$, the mean URs are larger than 50% for all point sources and cities with an emission rate larger than 2 MtC·yr⁻¹, but for achieving the same UR, an emission rate of at least 4 MtC·yr⁻¹ is needed for regional countryside emissions (Fig. 7c). The gap is even larger when using $\sigma_{\text{Budget}} = 50\%$, with mean URs that are systematically larger than 50% for annual emission budgets of point sources and cities larger than 2 MtC·yr⁻¹, but for annual emission budgets of regional countryside emissions larger than 7 MtC·yr⁻¹.



540 When aggregating the results for point sources, cities and countryside emissions at the regional scale, the relative prior
uncertainty becomes significantly smaller than the values used for individual sources since we assume that there is no
correlation between their uncertainties: the mean prior uncertainty for the regions is then of ~33% when assuming a 50%
prior error on the 6 h-budgets of point sources, cities and countryside areas which make these regions. And, the emission
threshold above which the UR for the regional budgets are larger than 50% becomes $10 \text{ MtC}\cdot\text{yr}^{-1}$ and $7 \text{ MtC}\cdot\text{yr}^{-1}$ when using
545 $\sigma_{\text{Budget}} = 50\%$ and 100% , respectively (Fig. 7d). These thresholds are larger than the ones corresponding to individual point
sources and cities as given above, but the overall performance of the inversion system at the regional scale is better with
respect to that of the point sources and cities when analyzing the relative posterior uncertainties: for $\sigma_{\text{Budget}} = 50\%$, the mean
value is of 22% for the total region budgets while it is of ~40 % for the point sources and cities budgets (Fig. A1).
The results for the different types of sources are shown for four regions of Belgium in Fig. 8. This figure provides an
550 illustration of the general results seen in Fig. 7. It shows that the URs for emissions from the largest urban areas (emitting
more than $2 \text{ MtC}\cdot\text{yr}^{-1}$) are as high as that for the overall emissions of their respective region although the budgets of
emissions from these urban areas are much smaller than that of their regions. As suggested above, smaller prior uncertainties
in the regional budgets lead to similar UR for cities and regions budgets even though the relative posterior uncertainties in
regional budgets are much smaller (Fig. 8b). When comparing point sources and cities which are characterized by the same
555 prior uncertainty, the relative magnitudes of the URs are determined by the relative magnitudes of the emissions: URs are
thus much higher for the largest urban areas than for point sources and cities that emit much less CO_2 . But, the comparison
between the URs and emissions of the main cities and countryside areas of the regions of East and West Vlaanderen
illustrates that, despite lower amplitudes, cities are better constrained than countryside areas. This is in agreement with the
enhanced capacity of the inversion system to monitor cities emissions with respect to more diffuse countryside emissions.
560 This figure also qualitatively illustrates the ability of the inversion system to separate neighbor emission sources: the point
source and city of Liège (left blue bar for the region of Liège in the figure) contained within the region of Liège are
characterized by significant UR even though the point source is within the city of Liege and its plume completely overlapped
with the plume from the rest of the city. We will analyze more systematically and quantitatively the capacity of the
framework to disentangle the information produced by neighbor sources in section 3.3.3.
565 The URs for the 6 h-emission budgets show an important variability over the 62 inversion days as illustrated in Fig. 7. When
using $\sigma_{\text{Budget}} = 50\%$, the standard deviations of the day-to-day variations of the URs for the point sources, cities and
countryside areas, are on average equal to ~12%, ~8.3% and 12.2%, respectively. These values are important with respect to
the temporal mean of the values of UR (26%, 16% and 27% when averaging across all the point sources, cities and
countryside areas respectively). These variations are associated to variations in the wind speed at the daily scale as it was
570 evidenced for the Paris case in section 3.2.1. However, when considering results for the months of March and May together,
they are also influenced by the time profiles of the anthropogenic emissions that are characterized by a strong decrease of
emissions between March and May due to the reduction of residential heating. Moreover, the UR variability is also
determined by the natural fluxes which are also very different from March to May, with large negative amplitudes in May



575 when they are dominated by the primary production and smaller positive amplitudes in March when they are mostly
restricted to the heterotrophic respiration. Furthermore, as the primary production related to photosynthetic processes is
mostly driven by the radiative forcing and then by the daily variation of the cloud cover, natural fluxes are also characterized
by a strong day-to-day variability during the month of May whereas in March, they are not because of a weak day-to-day
variability of heterotrophic respiration. Cross sensitivity studies comparing the influence of the above drivers (not shown),
indicate the predominant influence of the daily variability of the wind speed on the variability of UR for the anthropogenic
580 emissions estimates, for most sources. This conclusion should however be nuanced for some regions and countryside areas
where the scores of UR for the anthropogenic emission estimates is impacted by the inversion of the natural fluxes, and thus
by the variability of these fluxes, during the month of May (see section 3.3.2. below).

3.3.2. Impact of the uncertainties in the biogenic fluxes

The analysis of XCO₂ patterns produced by the different CO₂ fluxes (section 3.1) suggests that large signatures of the
585 biogenic fluxes in May could impact the monitoring of the anthropogenic emissions. In order to weigh the impact of the
uncertainties in biogenic fluxes, we conduct experiments where these uncertainties are ignored. In these experiments the
mean UR for the budgets of the regional and countryside anthropogenic emissions in May is equal to ~31% and ~41%
respectively (using $\sigma_{\text{Budget}}=50\%$). When accounting for uncertainties in biogenic fluxes, the mean URs decrease down to
~21% and ~31% respectively (Figs. 9c-d). This reveals some difficulty of the inversion system to separate countryside
590 emissions from biogenic fluxes which is also illustrated by the important anti-correlations (-40% on average) between the
corresponding *posterior* uncertainties. During May, the smaller amplitudes and rather diffuse nature of countryside
emissions with respect to natural fluxes (data not shown), and the overlapping of their atmospheric signatures (Fig. 2)
explain why the inversion system only has a limited ability to distinguish the countryside emissions. Oppositely, during
March, the smaller amplitudes of natural fluxes compared to countryside emissions (data not shown) explains why the
595 inversion can better filter the signature of countryside emissions from that of natural fluxes.

Contrarily to the UR for countryside emissions and regional budgets, the UR for the point sources and cities are hardly
impacted by the uncertainties in biogenic fluxes during the month of May, even when the emission budgets of these sources
are smaller than 1 MtC·yr⁻¹ (Figs. 9a and b), and even though these budgets are quantitatively lower than the absolute value
of the regional budgets of biogenic fluxes. Consistently, the *posterior* uncertainty in the inverted 6-hour budgets of the
600 emissions of cities or point sources is weakly correlated with that in the 6-hour budgets of biogenic fluxes in their respective
region (-2% and -5% on average for the cities and point sources respectively). Therefore, the visual inspection of Fig. 2 may
wrongly suggest that the plumes of the smallest point sources and cities controlled individually can hardly be separated from
the signature of biogenic fluxes. The differences in terms of spatial scales of the atmospheric signature appear to be the main
driver of the skill of the inversion for separating anthropogenic sources from biogenic fluxes.



605 3.3.3. Separation of the different anthropogenic emission sources

In order to estimate the ability of the inversion system to separately monitor anthropogenic sources whose atmospheric signals overlap, we focus on pairs of sources contained within a same region and we assess whether the sum of the variances (Var) associated to the inverted emissions for each source is comparable with the absolute value of their covariance (Cov), which is nearly systematically negative as a result of the uncertainty in the spatial attribution of emitted CO₂ to individual sources in the inversion. This criterion means, if the covariance is negative, that the variance associated to the ensemble of the two sources is much smaller than the sum of the variances associated to each source, given the mathematical expression governing the variance of the sum of two random variables X_a and X_b: $\text{Var}(X_a+X_b)=\text{Var}(X_a)+\text{Var}(X_b)+2*\text{cov}(X_a,X_b)$. In terms of inversion, this case describes the situation when a pair of sources is much better constrained than each of its individual sources ($\text{Var}(X_a+X_b)\ll\text{Var}(X_a)+\text{Var}(X_b)$), *i.e* when the inversion system does not entirely manage to disentangle overlapping signals and to constrain independently each source.

Figure 10 indicates that the system has an overall ability to independently constrain the different sources within a given region: point sources, cities, countryside areas, natural fluxes. In this figure indeed, the number of pairs of sources that are characterized by an important negative covariance term ($2*\text{cov}(X_a,X_b)$) compared to the sum of the individual variances ($\text{V}(X_a)+\text{V}(X_b)$) is much lower than the number of pairs of sources that are characterized by a relatively small covariance term. Only 20 pairs of sources out of a total of 890 pairs show a covariance term that is larger than 25% of the sum of the variances (squares below the blue line in Fig. 10a). Most pairs for which the inversion system may be unable to distinguish individual sources in a completely independent way consist in a point source and its surrounding urban or countryside area. Only one case consists in two point sources that are located close to each other near Karlsruhe in Germany and, no cases consist in pairs of urban/urban or urban/countryside areas. The 20 cases of less separable pairs of sources identified above could be associated to situations for which the inversion system could have difficulties to independently monitor two sources but this conclusion should be nuanced when all terms (sum of the variances and covariances) are small: four pairs of sources characterized by important negative correlations for example show an UR for each individual sources which is larger than 50% (squares in the top-right quadrant of the Fig. 10b). For these cases, the problem of distinction between the two sources applies to a moderate residual posterior uncertainty, and the inversion still gets a relatively precise estimate of the emissions. Moreover, a low covariance between pair of sources can often be explained by the lack of constraint on their total budget or on one of the two sources, rather by a good separation between the two sources. For example, pair of sources with an important UR for their total emissions and a small covariance while only one individual source is well constrained are represented by the top-left and bottom-right pairs of sources in Fig. 10b, (where the UR for the total is larger than 75% while one of the sources shows an UR lower than 20%). Pairs of sources characterized by relatively low values of covariance but small values of UR for both the total and the two sources are identified in the top-right quadrant of Fig. 10a and the down-left quadrant of Fig. 10b. These pairs are characterized by low individual sources and total emissions whose amplitudes are below the thresholds required by the inversion system to produce reliable estimates (see section 3.3.1.).



4. Discussion and conclusion

We have presented a new and comprehensive high-resolution atmospheric inversion system to assess the potential of the
640 satellite imagery of XCO₂ for the monitoring of anthropogenic emissions from local to national scales. This system has been
designed to deal with a wide range of different sources in terms of emission amplitude, distribution and spatial scales and to
account for the overlapping between the signatures from different anthropogenic sources and natural sources and sinks. To
cover the local and regional scales while mitigating computational costs, this inversion system is based on an atmospheric
transport model with a zoomed grid whose resolution ranges from 2 km in the most resolved domain to 50 km at its edges.
645 The area of highest resolution (2 km) encompasses regions where cities and point sources are inverted separately for their
hourly emission budget, i.e. that of Northern France, Belgium, the Netherlands, West Germany, Luxemburg and London.
Urban areas are delimited using a clustering algorithm and large industrial plants are selected based on an emission
threshold. In total, the system controls the hourly budgets of 303 different anthropogenic sources (plants, cities or regions),
the hourly budgets of 67 regional budgets of biogenic fluxes and the 6-hour average initial and lateral boundary conditions.

650

A performance simulation tool

The analytical formulation allows easily testing different scenarios for observation systems that monitor anthropogenic
emissions but, in this study, the OSSEs with the inversion framework have been performed in order to investigate the
655 potential of the satellite imagery of XCO₂ from helio-synchronous orbit only, depending on instrumental configurations or
other factors such as the wind or the amplitude of the emissions. Such a spaceborne imagery similar to CO₂M may become
the critical component of operational atmospheric inversion systems for the monitoring of CO₂ anthropogenic emissions.
These operational inversion systems will likely have to jointly assimilate data from many of the existing satellite missions,
from ground-based networks and from the planned spectro-imagers. Moreover, in addition to CO₂ concentrations, co-emitted
660 pollutants and radiocarbon should as well be assimilated. Ultimately, OSSEs would have to integrate all these components of
the observation system (Ciais et al., 2015; Pinty et al., 2017). However, we need OSSEs considering the spaceborne imagery
of XCO₂ as a stand-alone system to determine the instrumental parameters ensuring that this imagery can bring emission
estimates with sufficient coverage and accuracy so that it can serve as a backbone for such the emission operational
monitoring. Furthermore, in a context where there is a lack of ground based and spaceborne networks that are suitable for the
665 monitoring of CO₂ anthropogenic emissions, these OSSEs can help better understanding the needs in terms of
complementary observation components.

The analytical inversion system built for this study allows testing an important set of observational parameters and situations.
Once the atmospheric transport functions associated to the different emissions sources have been computed, the derivation of
the posterior uncertainties is fast and results can be delivered for a wide and detailed range of specifications on the spatial
670 resolution, precision and swath of the satellite XCO₂ images. Extending the study of Broquet et al. (2018), the sensitivities of



the inversion results to these three parameters have been tested on the example of the emissions of Paris (section 3.2.2.). We varied these parameters without accounting for current limitations in space technologies (or from cost issues) imposing potential trade-offs between their configurations. The impact of the wind speed on the determination of the 6-h and hourly budgets of the emissions is analyzed by assimilating images over different days of March and May. Finally, the flexibility of the inversion system also allowed testing the impact of the way a priori errors on the fluxes are prescribed.

The inversion framework produces curves of sensitivity that give several qualitative and quantitative insights into the optimal configurations of the satellite imagery. If we consider the monitoring of the Paris emissions, the impact of the swath on the results is limited for swaths larger than 400 km (section 3.2.2 and Fig. 4). As the megacity of Paris produces plumes whose intensity and extension are amongst the highest with respect to anthropogenic emissions sources in Western Europe, this supports the use of a swath close to 400 km in order to remove the influence of this instrument parameter on the ability to catch the full extent of plumes from targeted sources in the center of the satellite field of view.

The study of the UR for the Paris emissions indicates (i) that a $4 \text{ km} \times 4 \text{ km}$ spatial resolution is sufficient, provided that the precision at this spatial resolution is very high, and (ii) that the inversion hardly makes use of patterns at finer spatial resolution. However, as discussed in section 3.2., that might come from the relatively large extent of the plume from Paris, and from its distances from other major plumes. We have thus extended the analysis of the sensitivity to the observation spatial resolution and precision to all the days of March and May and to the ensemble of controlled regional, city and local sources (as for the analysis in section 3.3) using a reduced set of resolutions and precisions to be tested. The results are displayed in Fig. 11. This experiment confirms that results for point sources and narrow cities are more sensitive to the availability of the information at the reference resolution of 2 km than that for Paris. The UR for point sources and cities emitting less than $2 \text{ MtC}\cdot\text{yr}^{-1}$ is larger with a spatial resolution of $2 \text{ km} \times 2 \text{ km}$ and a precision of 1.2 ppm than with a spatial resolution of $4 \text{ km} \times 4 \text{ km}$ and a precision of 0.6 ppm, (i.e. with the same precision at 4 km resolution but without information about the patterns at scales finer than 4 km). However, the differences are not really significant, and Fig. 11 tends to confirm that a spatial resolution of $4 \text{ km} \times 4 \text{ km}$ would be fine if achieving a very good precision: typically, 0.3 ppm if willing to get the results from the reference configuration of the observation with 2 km resolution and 0.6 ppm precision. With a $2 \text{ km} \times 2 \text{ km}$ resolution, the mean URs for all type of emissions would increase on average by $10.1 \pm 1.5\%$ if the precision increases by a twofold factor (from $\sigma = 1.2 \text{ ppm}$ to 0.6 ppm and from 0.6 ppm to 0.3 ppm). While this represent a dramatic increase of the UR when changing the precision from 1.2 ppm to 0.6 ppm, the relative impact is smaller from 0.6 to 0.3 ppm and the reference value of 0.6 ppm precision at 2 km resolution appear to be a balanced option. Finally, the results for the Paris case point out that, at the reference precision of 0.6 ppm, the performance of the inversion system would be nearly equivalent at the resolutions of $2 \text{ km} \times 2 \text{ km}$ and $2 \text{ km} \times 3 \text{ km}$ (Fig. 4). The spatial resolution could thus be relaxed to $2 \text{ km} \times 3 \text{ km}$ compared to the reference resolution without degrading much the precision of the inversions.

If we consider the monitoring of the Paris emissions, the impact of the swath on the results is limited for swaths larger than 400 km (section 3.2.2 and Fig. 4). As the megacity of Paris produces plumes whose intensity and extension are amongst the highest with respect to anthropogenic emissions sources in Western Europe, this supports the use of a swath close to 400 km



705 in order to remove the influence of this instrument parameter on the ability to catch the full extent of plumes from targeted
sources in the center of the satellite field of view. However, a narrower swath would be sufficient for the large majority of
cities which emit less than Paris, and thus have shorter plumes. This would impact the monitoring of the large megacities
emitting more than 10 MtC/yr like Paris, which represent more than 9% of the emissions from cities and power plants over
the globe (Wang et al., 2020), but section 3.2.2 shows that this impact is limited for Paris in most meteorological conditions
710 as long as it is larger than 250 km (90% of the cases for the 62 days of inversion, not shown). A general conclusion from
these results is that the swath is a less critical parameter than the pixel precision and resolution.

Overall, these results support the reference configurations for the pixel resolution and precision and for the swath width that
broadly correspond to the current ones for the CO2M mission, even though they suggest a relaxation of the spatial resolution
to 2 km x 3 km and an extension of the swath up to 400 km. However, since this study does not account for technical and
715 cost trade-offs between these parameters, it cannot provide a full assessment for their combination. Furthermore, by flying a
satellite any day over the areas of interest in the sensitivity tests, we restrained the role of the swath to covering a more or
less important portion of the plumes, with a lack of sensitivity when the swath exceeds the plume length or when the wind
blows along the satellite track. In practice, a critical role of larger swaths (like that of more satellites in a constellation) is to
increase the number of situations for which the plume from a given city can be seen, which is ignored in this study. Finally,
720 the spatial resolution could also play a role when accounting for cloud cover since it could help increasing the spatial
coverage. A more realistic simulation of the observation sampling by specific missions or constellations, with one or several
satellites following real tracks and including the impact of cloud coverage, and some realistic technical constraints between
the parameters, is needed to fully assess the right balance between higher precision, finer spatial resolution and larger
swaths.

725
Ability to monitor anthropogenic emissions at the regional, city and local scales

At first, a qualitative overview of the atmospheric signatures could imply that the ability of the inversion system to quantify
the budgets of emissions from most of the 84 large point sources and from the two megacities of Paris and London should be
730 much larger than for smaller individual cities, and that countryside emissions should hardly be constrained by the inversion
(section 3.1). The quantitative OSSE analysis described in section 3.3. however shows that the capacity of detection of the
inversion system is equivalent for point sources and cities: uncertainties on both type of sources are reduced on average by
more than 50% above an emission threshold of 2 MtC·yr⁻¹ when the resolution and precision of the satellite data are equal to
2 km × 2 km and to 0.6 ppm respectively, and when the prior uncertainties on the fluxes have been set to 50% of the 6 h-
735 budgets (section 3.3.1). With the same parameters, the threshold is much higher (~10 MtC·yr⁻¹) for the anthropogenic
emissions of the countryside areas and of the whole regions but, for these type of sources, the overall performance of the
inversion system is still comparable to that for point sources and cities: for the 67 regions considered in this study, the mean
URs for the total emissions and for the countryside emissions are of 37% and 27.4% respectively (section 3.3.1). The



740 relatively lower performance of the inversion system to monitor the countryside and regional anthropogenic emissions could be partly related to the impact of the biogenic fluxes on the determination of these types of emission sources contrary to the point sources and cities (section 3.3.2).

We have also addressed the capacity of the inversion system to deal with the overlapping of XCO₂ plumes produced by nearby sources (section 3.3.3). As satellite images give snapshots of the XCO₂ distribution at a given time (11:00) and as atmospheric transport mixes the contribution of the different sources over the 6 hours before the satellite overpass, it is
745 important to assess the ability of the inversion system to disentangle the information coming from different sources at different times. With the hypothesis adopted in this study, most point sources and cities can be independently monitored by the inversion system. This ability could be partly related to the high-resolution modeling that allows describing and catching the fine scale patterns of the XCO₂ signatures of the point sources even if the inversion is weakly sensitive to patterns at scales <4km (Fig. 11).

750 Beyond the capacity to monitor separately the emissions of point sources, urban and countryside areas, the additional benefit of separately controlling these emissions within a given region is the mitigation of the so-called aggregation errors (Kaminski et al., 2001) when inverting the total budget of a region. In analytical inversions, these errors arise when a control of the emissions at a too coarse resolution limits too much the ability to fit the actual spatial distribution of the emission and of the concentrations. These errors are evidenced for our study by inverting regional budgets without considering any
755 internal separation into cities, point sources or countryside areas in the control vector: the results are indeed significantly and wrongly more optimistic than the ones obtained with the inversions that consider this subdivision (Fig. A2).

An optimistic framework

760 This study aims at assessing the projection of only the sampling and observation random noise into the emission estimates. It combines optimistic assumptions that prevent from assuming that the level of posterior uncertainties achieved in the OSSEs here should correspond to that of the inversions with real data. The ability of the inversion system to separately monitor point sources and cities (section 3.3.3) and to quantify regional budgets of diffuse emissions is partly due to the underlying assumption made in this study that the atmospheric transport is perfectly known. We ignored the transport modeling errors
765 and implicitly supposed that the position and extent of the city or point sources XCO₂ plumes are perfectly simulated. Accounting for the transport modeling errors by assuming that they can be described as a random noise uncorrelated in space and time, as is usually done in atmospheric inversions, would not fundamentally change the results of this study. The impact of such an error would be equivalent to decreasing the precision of the observation. However, as a consequence of errors in the wind speed and direction, or in the structure of the transport model, the simulation of narrow and localized plumes can
770 poorly match the actual ones and strongly affect the inversion of the emissions from point sources and cities. The actual signature of diffuse emissions could also be different in terms of shape, and extent from the actual one. An inversion procedure that would simultaneously control both transport parameters and CO₂ emissions within a coupled meteorological-



CO₂ transport model (Kang et al., 2011) may partially address these issues although it would greatly increase the complexity of the inversion, in particular by introducing potentially large non-linearities in the observation operator. New methods based on imagery processing (Corpetti et al., 2009), plume detection (Kuhlmann et al., 2019), Gaussian plume modeling (Nassar et al., 2016) or direct computation of fluxes through detected plumes may also help overcoming realistic transport uncertainties to invert the emissions corresponding to point sources and cities (Varon et al., 2018). However, these methods may hardly deal with diffuse emissions whose signatures have low amplitudes, and should be difficult to detect in XCO₂ images. The recovering of countryside emissions and of regional budgets of the emissions may thus be optimistic in this study.

Moreover, the configuration of our inversion system uses many of the traditional assumptions of inversion systems among which the rather simple characterization of some sources of uncertainties by Gaussian distributions, which may underestimate their impact in the inversions. Furthermore, some sources of observation errors, such as the so-called systematic errors which bear spatial correlations, are purposely ignored in the present study. Such errors exacerbate the problem of the identification of the signature of point source, city to diffuse emissions in addition to have a larger error budget than random noise on the spatial scales of such signatures. There is a clear need to assess the impact of such correlated errors with a similar system than the one presented in this study. Lastly, the extent of the observation sampling is made rather optimistic by ignoring cloud cover. In a general way, the results of this study could be seen as optimistic and as an upper limit of the skill of the inversions using satellite images only but, also as good indicators of the sensitivity of the uncertainty reduction to various parameters and drivers.

Broquet et al. (2018) provided insights into the impact of cloud cover and systematic errors in the XCO₂ images. They used realistic simulations of satellite samplings and errors made for the CarbonSat mission by (Buchwitz et al. 2013). Results have indicated that, when accounting for cloud cover, the satellite data could efficiently constrain emissions from Paris only ~20 days per year, and that the impact of the systematic errors anticipated for that mission is such that the system would hardly be able to reduce errors in the emission estimates if such errors are not filtered or controlled for. Efforts have been made to limit the amplitude of such errors in the concept of the new CO2M mission. Our new inversion framework allows accounting for a realistic simulation of the observation sampling and errors. In particular, future studies will integrate realistic simulations of observation sampling and errors from different concepts of spaceborne imagery, based on radiative transfer inverse modeling applied to realistic fields of surface and atmospheric conditions and instrumental specifications.

Exploiting further capabilities of the inversion framework: potential of complementary observation systems and results at larger temporal scales

Our analysis is restricted to a window from 5:00 to 11:00 corresponding to the period which might be constrained by the satellite observation from a heliosynchronous satellite with 11:00 local overpass time. This provides little information about the capacity of the inversion system to monitor daily to monthly budgets. To address this need and improve the results of the



inversions, the modularity of our data assimilation framework could integrate multiple streams of data in order to increase the temporal and spatial coverage of the information (Moore et al., 2018; O'Brien et al., 2016).

In future studies, our inversion system could also integrate more realistic hypotheses concerning the description of the prior uncertainties on the emissions. Uncertainties in inventories are indeed difficult to characterize and this study assumed, rather arbitrarily, that the relative error for the 6h budgets was of 50% or 100% (section 2.4). We also assumed that the prior uncertainties had low temporal correlations, i.e. correlation over timescales of less than 6h, and we neglected the spatial correlations between the budgets for the different point sources, cities and countryside areas. Actual anthropogenic emissions and inventories have complex cycles at daily and weekly scales together with a large temporal and spatial variability. However, we can expect some stronger spatial and temporal connections than assumed in this study, which would increase the transfer of information from the atmospheric observations, *i.e.* both the uncertainty reduction for the sources and time windows covered by the observations, and the uncertainty reduction for other sources, time windows, and for large spatial and temporal scales.

Acknowledgements

This work was supported by the Chaire Industrielle Trace ANR-17-CHIN-0004-01 cofunded by the ANR French national research agency, THALES ALENIA SPACE, SUEZ-Environnement, and TOTAL-Raffinage Chimie. The authors are grateful for TAS partners, in particular Sandrine Mathieu, LMD partners, in particular Vincent Cassé, Cyril Crevoisier and Olivier Chomette, and colleagues from LSCE: Yilong Wang, Elise Potier and all the Chaire TRACE team for fruitful discussions.

References

- Bocquet, M., Wu, L. and Chevallier, F.: Bayesian design of control space for optimal assimilation of observations. Part I: Consistent multiscale formalism, *Quarterly Journal of the Royal Meteorological Society*, 137(658), 1340-1356, 2011.
- Bovensmann, H., Buchwitz, M., Burrows, J. P., Reuter, M., Krings, T., Gerilowski, K., Schneising, O., Heymann, J., Tretner, A., and Erzinger, J.: A remote sensing technique for global monitoring of power plant CO₂ emissions from space and related applications, *Atmos. Meas. Tech.*, 3, 781–811, <https://doi.org/10.5194/amt-3-781-2010>, 2010.
- Buchwitz, M., Reuter, M., Bovensmann, H., Pillai, D., Heymann, J., Schneising, O., Rozanov, V., Krings, T., Burrows, J. P., Boesch, H., Gerbig, C., Meijer, Y., and Löscher, A.: Carbon Monitoring Satellite (CarbonSat): assessment of scattering related atmospheric CO₂ and CH₄ retrieval errors and first results on implications for inferring city CO₂ emissions, *Atmos. Meas. Tech. Discuss.*, 6, 4769–4850, [doi:10.5194/amt-d-6-4769-2013](https://doi.org/10.5194/amt-d-6-4769-2013), 2013.



- Bréon, F. M., Broquet, G., Puygrenier, V., Chevallier, F., Xueref-Remy, I., Ramonet, M., Dieudonné, E., Lopez, M.,
835 Schmidt, M., Perrussel, O., and Ciais, P.: An attempt at estimating Paris area CO₂ emissions from atmospheric concentration
measurements, *Atmos. Chem. Phys.*, 15, 1707–1724, <https://doi.org/10.5194/acp-15-1707-2015>, 2015.
- Broquet, G., Bréon, F.M., Renault, E., Buchwitz, M., Reuter, M., Bovensmann, H., Chevallier, F., Wu, L., and Ciais, P.: The
potential of satellite spectro-imagery for monitoring CO₂ emissions from large cities, *Atmos. Meas. Tech.*, 11, 681–708,
<https://doi.org/10.5194/amt-11-681-2018>, 2018.
- 840 Buchwitz, M., Reuter, M., Bovensmann, H., Pillai, D., Heymann, J., Schneising, O., Rozanov, V., Krings, T., Burrows, J. P.,
Boesch, H., Gerbig, C., Meijer, Y., and Löscher, A.: Carbon Monitoring Satellite (CarbonSat): assessment of atmospheric
CO₂ and CH₄ retrieval errors by error parameterization, *Atmos. Meas. Tech.*, 6, 3477–3500, <https://doi.org/10.5194/amt-6-3477-2013>, 2013.
- Buchwitz, M., Reuter, M., Bovensmann, H., Pillai, D., Heymann, J., Schneising, O. and Gerbig, C.: Carbon Monitoring
845 Satellite (CarbonSat): assessment of scattering related atmospheric CO₂ and CH₄ retrieval errors and first results on
implications for inferring city CO₂ emissions, *Atmospheric Measurement Techniques*, 6(12), 3477-3500, 2013.
- Chevallier, F.: Description of the CO₂ inversion production chain. CAMS deliverable CAMS73 _2015SC2 _D73.1.5.5
_201703_CO2 inversion production chain_v1. <http://atmosphere.copernicus.eu/>, 2017a.
- Chevallier, F.: Validation report for the inverted CO₂ fluxes, v16r1. CAMS deliverable CAMS73_2015SC2_D73.1.4.2-
850 1979-2016-v1_201707. <http://atmosphere.copernicus.eu/>, 2017b.
- Chevallier, F., Feng, L., Bösch, H., Palmer, P. I., Rayner, P. J.: On the impact of transport model errors for the estimation of
CO₂ surface fluxes from GOSAT observations, *Geophysical Research Letters*, 37(21), 2011.
- Ciais, P., Crisp, D., Denier van der Gon, H. A. C., Engelen, R., Heimann, M., Janssens-Maenhout, G., Rayner, P., and
Scholze, M.: Towards a European Operational Observing System to Monitor Fossil CO₂ emissions, European Commission
855 Directorate-General for Internal Market, Industry, Entrepreneurship and SMEs Directorate I – Space Policy, Copernicus and
Defence, Brussels, Belgium, 2015.
- Corpetti, T., Héas, P., Mémin, E., Papadakis, N. : Pressure image assimilation for atmospheric motion estimation. *Tellus A:
Dynamic Meteorology and Oceanography*, 61(1), 160-178, 2009.
- Houweling, S., Aben, I., Breon, F. M., Chevallier, F., Deutscher, N., Engelen, R., Marshall, J.: The importance of transport
860 model uncertainties for the estimation of CO₂ sources and sinks using satellite measurements, *Atmospheric chemistry and
physics*, 10(20), 9981-9992, 2010.
- Inness, A., Ades, M., Agustí-Panareda, A., Barré, J., Benedictow, A., Blechschmidt, A. M.,, and Huijnen, V.: The CAMS
reanalysis of atmospheric composition, *Atmospheric Chemistry and Physics*, 19(6), 3515-3556, 2019.
- Kaminski, T., Rayner, P. J., Heimann, M., Enting, I. G.: On aggregation errors in atmospheric transport inversions, *Journal
865 of Geophysical Research, Atmospheres*, 106(D5), 4703-4715, 2001.
- Kang, J. S., Kalnay, E., Liu, J., Fung, I., Miyoshi, T., and Ide, K.: “Variable localization” in an ensemble Kalman filter:
Application to the carbon cycle data assimilation. *Journal of Geophysical Research: Atmospheres*, 116(D9), 2011.



- Kuhlmann, G., Broquet, G., Marshall, J., Clément, V., Löscher, A., Meijer, Y., and Brunner, D.: Detectability of CO₂ emission plumes of cities and power plants with the Copernicus Anthropogenic CO₂ Monitoring (CO2M) mission, 870 *Atmos. Meas. Tech. Discuss.*, <https://doi.org/10.5194/amt-2019-180>, in review, 2019.
- Mahadevan, P., Wofsy, S. C., Matross, D. M., Xiao, X., Dunn, A. L., Lin, J. C., ... & Gottlieb, E. W.: A satellite-based biosphere parameterization for net ecosystem CO₂ exchange: Vegetation Photosynthesis and Respiration Model (VPRM), *Global Biogeochemical Cycles*, 22(2), 2008.
- Moore III, B., Crowell, S. M., Rayner, P. J., Kumer, J., O'Dell, C. W., O'Brien, D. and Lemen, J.: The potential of the 875 geostationary carbon cycle observatory (GeoCarb) to provide multi-scale constraints on the carbon cycle in the Americas, *Frontiers in Environmental Science*, 6, 109, 2018.
- Nassar, R., Hill, T. G., McLinden, C. A., Wunch, D., Jones, D. B. A., and Crisp, D.: Quantifying CO₂ Emissions from Individual Power Plants From Space, *Geophys. Res. Lett.*, 44, 10045–10053, <https://doi.org/10.1002/2017GL074702>, 2017.
- O'Brien, D. M., Polonsky, I. N., Utembe, S. R., and Rayner, P. J.: Potential of a geostationary geoCARB mission to estimate 880 surface emissions of CO₂, CH₄ and CO in a polluted urban environment: case study shanghai, *Atmospheric Measurement Techniques*, 9(9), 4633-4654, 2016.
- Oda, T. and Maksyutov, S.: ODIAC Fossil Fuel CO₂ Emissions Dataset, Center for Global Environmental Research National Institute for Environmental Studies, <https://doi.org/10.17595/20170411.001>, 2015.
- Parkinson, C. L., Ward, A., and King, M. D.: Earth science reference handbook: a guide to NASA's earth science program and earth observing satellite missions, National Aeronautics and Space Administration, 277, 2006.
- 885 Patra, P., Law, R. M., Peters, W., Rödenbeck, C., Takigawa, M., Aulagnier, C., and Bruhwiler, L.: TransCom model simulations of hourly atmospheric CO₂: Analysis of synoptic-scale variations for the period 2002–2003, *Global Biogeochemical Cycles*, 22(4), 2008.
- Pillai, D., Buchwitz, M., Gerbig, C., Koch, T., Reuter, M., Bovensmann, H., Marshall, J., and Burrows, J. P.: Tracking city 890 CO₂ emissions from space using a high-resolution inverse modeling approach: a case study for Berlin, Germany, *Atmos. Chem. Phys.*, 16, 9591–9610, <https://doi.org/10.5194/acp-16-9591-2016>, 2016.
- Pinty, B., Janssens-Maenhout, G., Dowell, M., Zunker, H., Brunhes, T., Ciais, P., ... , and Engelen, R.: An operational anthropogenic CO₂ emissions monitoring and verification support capacity. Baseline requirements, model components and functional architecture, doi: 10.2760/08644, European Commission Joint Research Centre, EUR 28736 EN, 2017.
- 895 Pregger, T., Scholz, Y., et Friedrich, R.: Documentation of the anthropogenic GHG emission data for Europe provided in the Frame of CarboEurope GHG and CarboEurope IP. *Institut für Energiewirtschaft und Rationelle Energieanwendung, Universität Stuttgart, Stuttgart, Germany, 2007.*
- Sarmiento, D., Shepson, P., Sweeney, C., Turnbull, J., and Wu, K.: High-resolution atmospheric inversion of urban CO₂ emissions during the dormant season of the Indianapolis Flux Experiment (INFLUX), *J. Geophys. Res.*, 121, 2015JD024473, 900 <https://doi.org/10.1002/2015JD024473>, 2016.



Schwandner, F. M., Gunson, M. R., Miller, C. E., Carn, S. A., Eldering, A., Krings, T., ..., and O'Dell, C. W.: Spaceborne detection of localized carbon dioxide sources, *Science*, 358(6360), eaam5782, 2017.

Staufer, J., Broquet, G., Bréon, F.-M., Puygrenier, V., Chevallier, F., Xueref-Rémy, I., Dieudonné, E., Lopez, M., Schmidt, M., Ramonet, M., Perrussel, O., Lac, C., Wu, L., and Ciais, P.: The first 1-year-long estimate of the Paris region fossil fuel CO₂ emissions based on atmospheric inversion, *Atmos. Chem. Phys.*, 16, 14703–14726, <https://doi.org/10.5194/acp-16-14703-2016>, 2016.

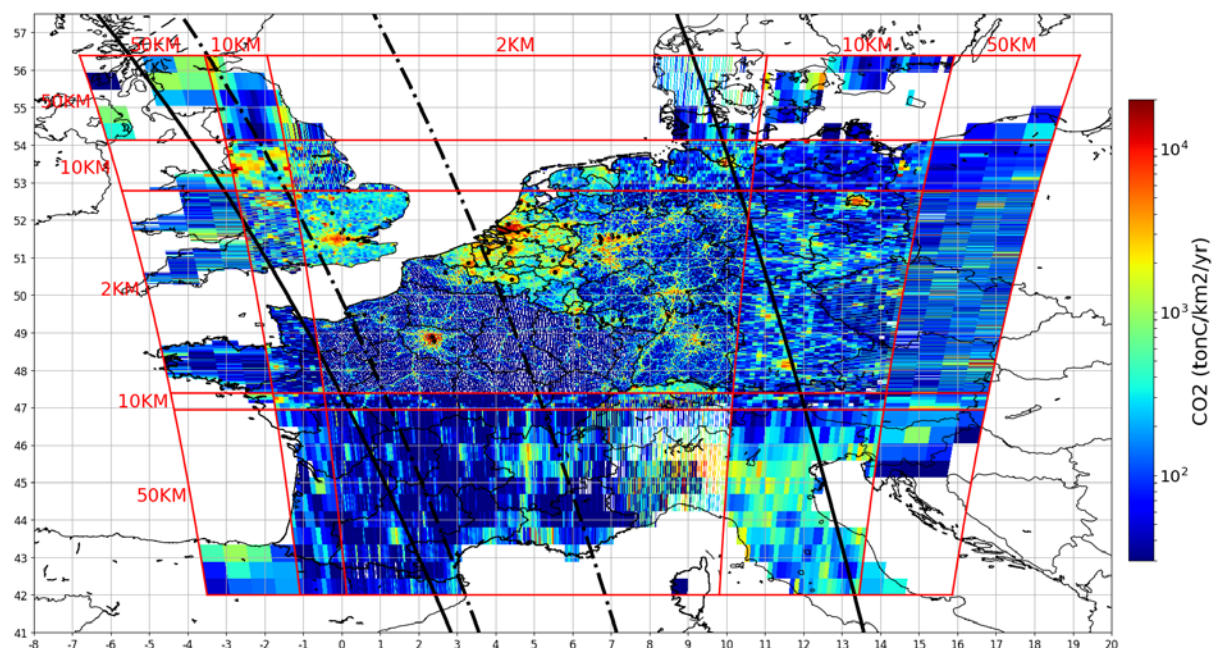
Stockman, G. Shapiro, L.G.: *Computer Vision* (1st ed.). Prentice Hall PTR, Upper Saddle River, NJ, USA, 2001.

Tarantola, A.: *Inverse Problem Theory: Methods for Data Fitting and Parameter Estimation*, Elsevier, 1987.

Thiruchittampalam, B.: PhD thesis Entwicklung und Anwendung von Methoden und Modellen zur Berechnung von räumlich und zeitlich hoch aufgelösten Emissionen in Europa, PhD Thesis at the University Stuttgart IER, Band 118, 2012.

Varon, D. J., Jacob, D. J., McKeever, J., Jervis, D., Durak, B. O., Xia, Y., ..., Huang, Y.: Quantifying methane point sources from fine-scale satellite observations of atmospheric methane plumes. *Atmos Meas Tech*, 11, 5673-5686, 2018.

Wang, Y., Broquet, G., Bréon, F.-M., Lepsinas, F., Buchwitz, M., Reuter, M., Meijer, Y., Loescher, A., Janssens-Maenhout, G., Zheng, B., and Ciais, P.: PMIF v1.0: an inversion system to estimate the potential of satellite observations to monitor fossil fuel CO₂ emissions over the globe, *Geosci. Model Dev. Discuss.*, <https://doi.org/10.5194/gmd-2019-326>, in review, 2020.



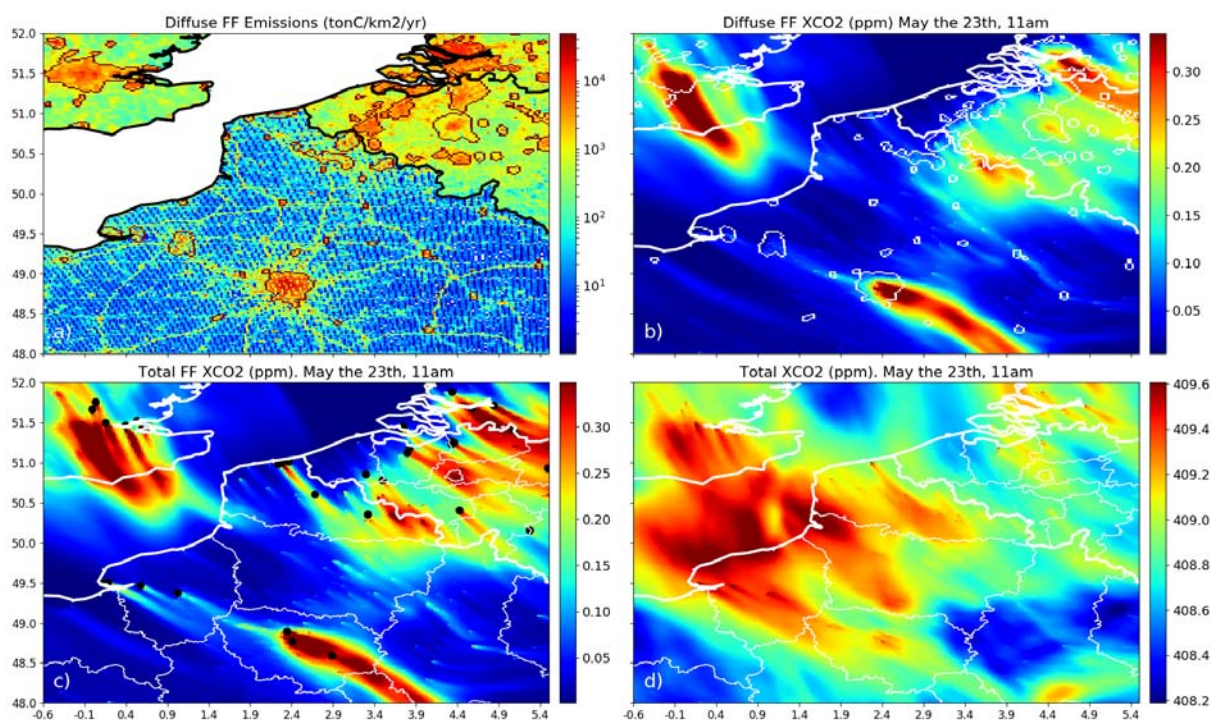
920 **Figure 1:** Maps of the IER annual emissions interpolated over the domain of the CHIMERE model. Point sources are indicated by black dots and administrative regions by thin black lines. The grid of the model is defined by sub-domains with several resolutions



($r \times s \text{ km}^2$ where r and $s=2, 10$ or 50 km) and whose boundaries are represented by the red lines. The thick black lines depict the edges of the satellite tracks corresponding to the synthetic data used in this study (300 km swath: dash-dotted line, 900 km swath: solid line).

925

930

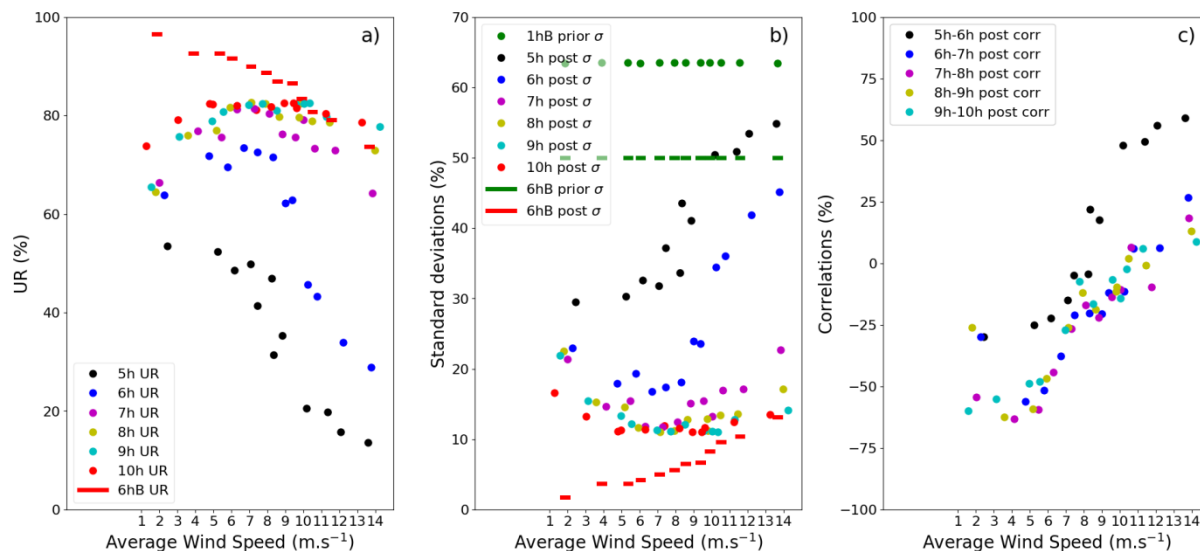


935 **Figure 2:** IER emission maps interpolated over Northern France, Western Belgium and the London area (a). We have represented the anthropogenic emission sources without point sources ("area emissions"). Red curves depict the boundaries of the city clusters defined by a pattern recognition algorithm (Section 2.2.3.). Panels (b) and (c) show the simulations of XCO₂ (ppm) on May the 23rd at 11am that are produced respectively by the area and total anthropogenic emissions between 5:00 and 11:00. Point sources are indicated by black dots in panel (c). In panel (d), simulations of XCO₂ (ppm) on May the 23rd at 11am that are produced altogether by the anthropogenic, natural and boundary fluxes between 5:00 and 11:00. For the sake of clarity, these figures do not show the whole 2 km-resolution sub-domain of CHIMERE, but illustrate the patterns seen over this subdomain well.

940

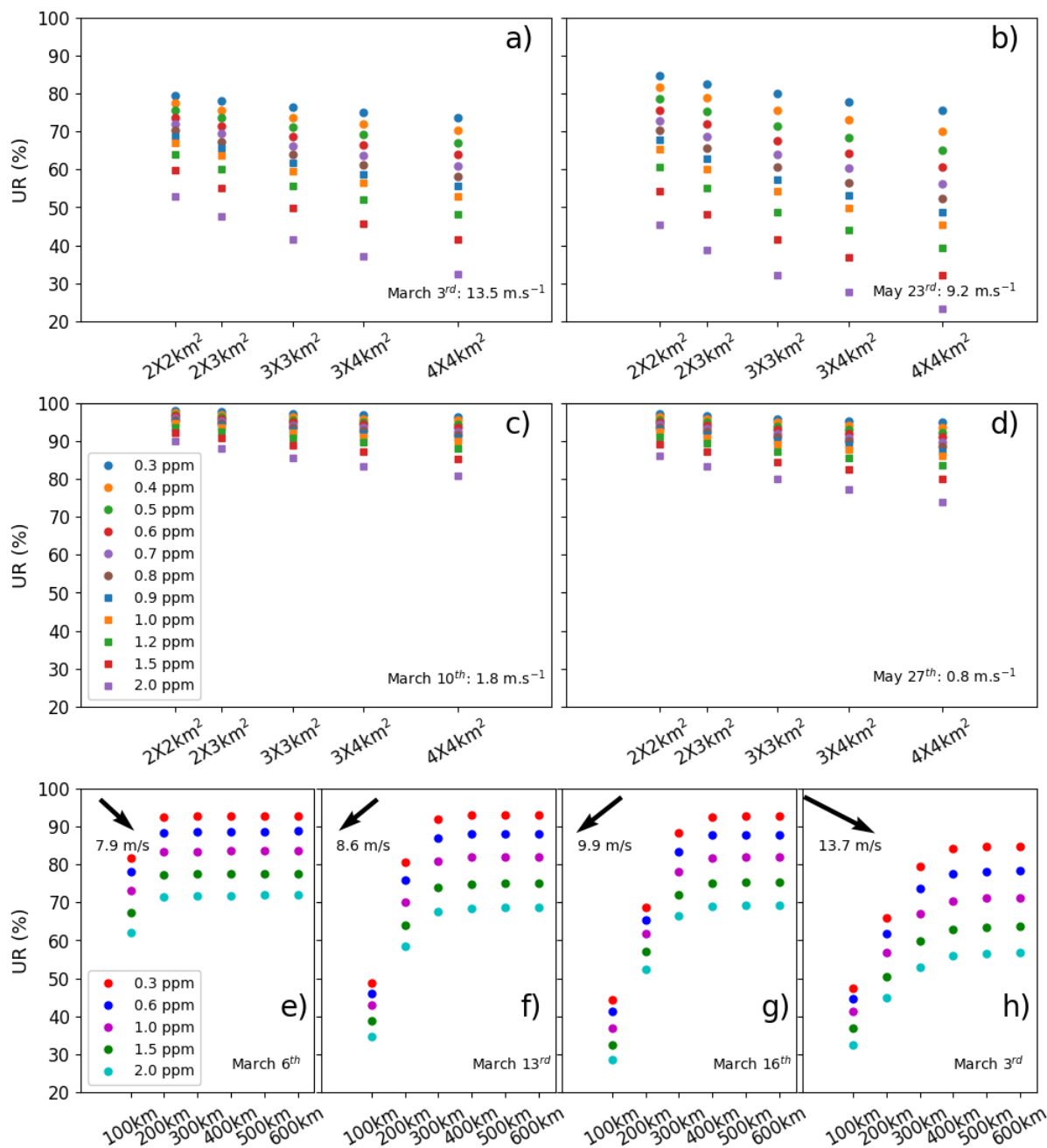


945



950

Figure 3: Uncertainty Reductions (UR) from a 50% prior uncertainty on the 6 h-budgets of the Paris emissions for 12 days characterized by different average wind speeds over Paris (a). URs for hourly and 6 h-budgets of the Paris emissions are shown by color dots and red segments respectively. In panel (b) are shown prior vs. posterior uncertainties on 1h-emissions (color dots) and 6h-emissions of Paris (green and red segments). In panels (a,b), the colors of the dots represent the hour of the corresponding 1 h-budget; the green dots are for the prior uncertainties on the 1 h-emissions (1hB prior σ) which are derived from 50% prior errors on the 6h-budgets (6hB prior σ) and by considering temporal prior correlations of 3 hours. Panel (c) shows correlations between posterior uncertainties in 2 consecutive 1 h-emissions (color dots). Results are computed with a retrieval resolution of 2 km \times 2 km, a precision of 0.6 ppm and a swath of 300 km.



955

Figure 4: Uncertainty Reductions (UR) from a 50% prior uncertainty for the 6 h-budgets of the Paris emissions. In panels (a)-(d), results are displayed for 4 different days characterized by different wind speeds, for different spatial resolutions of the satellite data (x-axis) and for different precisions (color markers). For the panels (a)-(d), results are generated by considering a swath of 300 km. In panels (e)-(h), results are displayed for 4 different days characterized by different wind speeds, for different swaths of the satellite data (x-axis), for different precisions (color markers) and for a resolution of 2 km by 2 km.

960

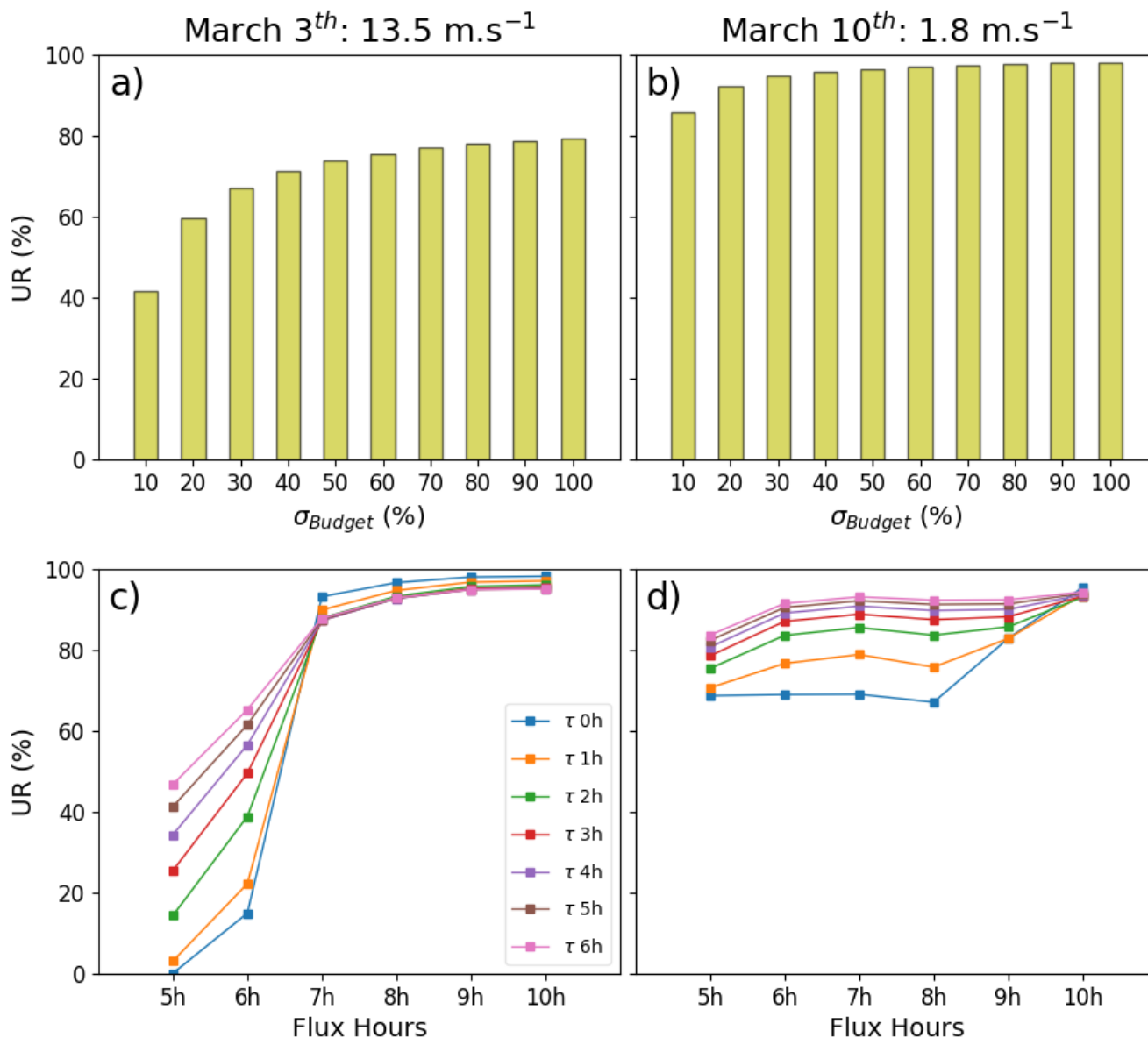
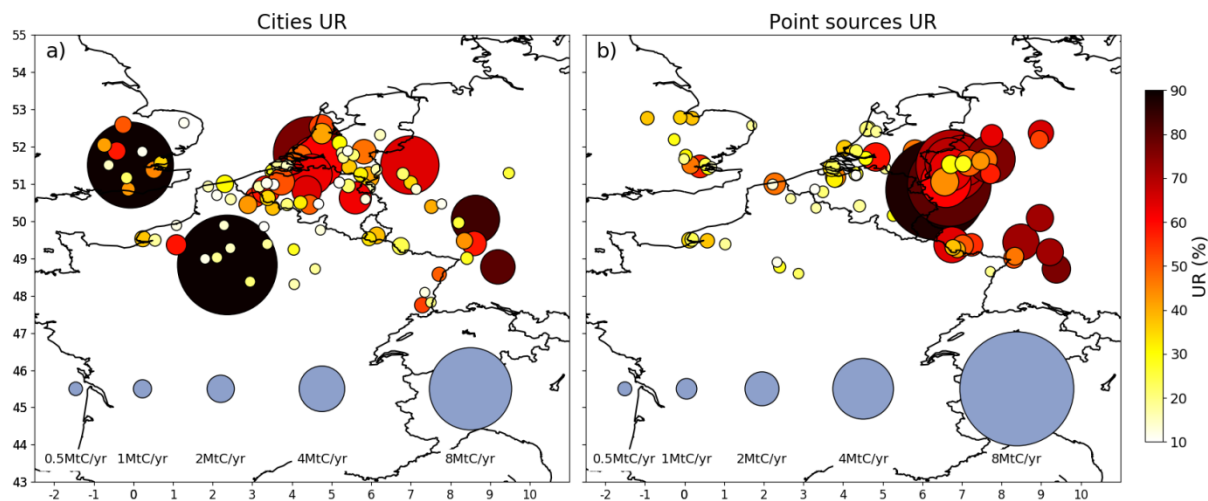


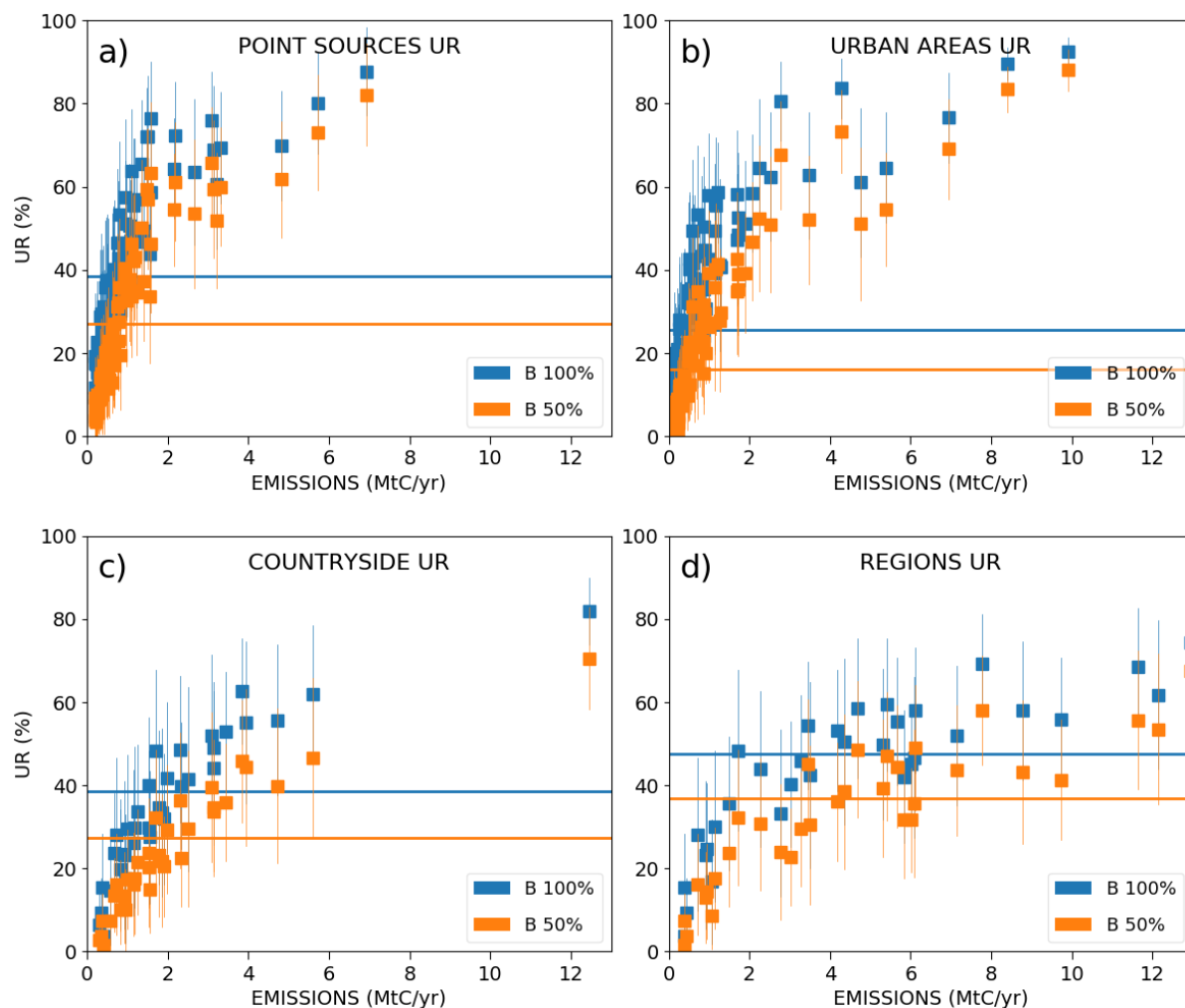
Figure 5: Uncertainty Reductions (UR) as a function of the prior uncertainty (x-axis) for 6 h-budgets of the Paris emissions (a,b). Correlations between the prior errors on hourly emissions have a temporal length of 3 hours (see section 2.4). Panels (c,d) show the URs for the hourly emissions between 5h and 11h (x-axis) for several temporal lengths defining the correlations between prior errors on hourly emissions (color dots), legend “ τ 0h” being for an absence of such correlations. Prior uncertainties on 6 h-budgets of Paris emissions are taken equal to 50% in panels (c,d). Columns represent 2 different inversion days: March 2016 the 3rd (strong wind) and March 2016 the 10th (low wind). All inversion results are computed with a retrieval resolution of 2 km \times 2 km, a precision of 0.6 ppm and a swath of 300 km.

965

970



975 **Figure 6: Mean Uncertainty Reductions (UR) for some city clusters (a) and some point sources (b) across the 62 inversion results of the days of March and May 2016. The areas and colors of the disks represent the annual emissions ($\text{MtC}\cdot\text{yr}^{-1}$) and the URs (%) respectively. The inversions are performed with a retrieval resolution of $2\text{ km} \times 2\text{ km}$, a precision of 0.6 ppm and a swath of 900 km . Prior uncertainties on 6h-budgets of clusters and point sources emissions are taken equal to 50% and prior error correlations have a temporal length of 3 hours .**



980

985

990

Figure 7: Mean values and standard deviations of the Uncertainty Reductions (UR) for the emissions of point sources (a), urban areas (b), countryside areas (c), and regions (d) across the 62 inversion results of the days of March and May 2016. The lines represent the averages of the temporal mean values across all sources of a given type. The emitting areas are chosen within the 2-km-resolution domain of the model so that they are covered by the satellite track in order to avoid swath effects. Results are given as a function of the annual emissions (x-axis) of the emitting areas. The inversions are performed with a retrieval resolution of 2 km × 2 km, a precision of 0.6 ppm and a swath of 900 km. Prior uncertainties on the 6 h-budgets of the point sources, urban and countryside areas are taken equal to 50% (orange squares) and to 100% (blue squares). Prior uncertainties on the regional budgets are derived by aggregation of the prior uncertainties on their constituent emitting sources for both cases. Prior error correlations between hourly emissions have a temporal length of 3 hours.

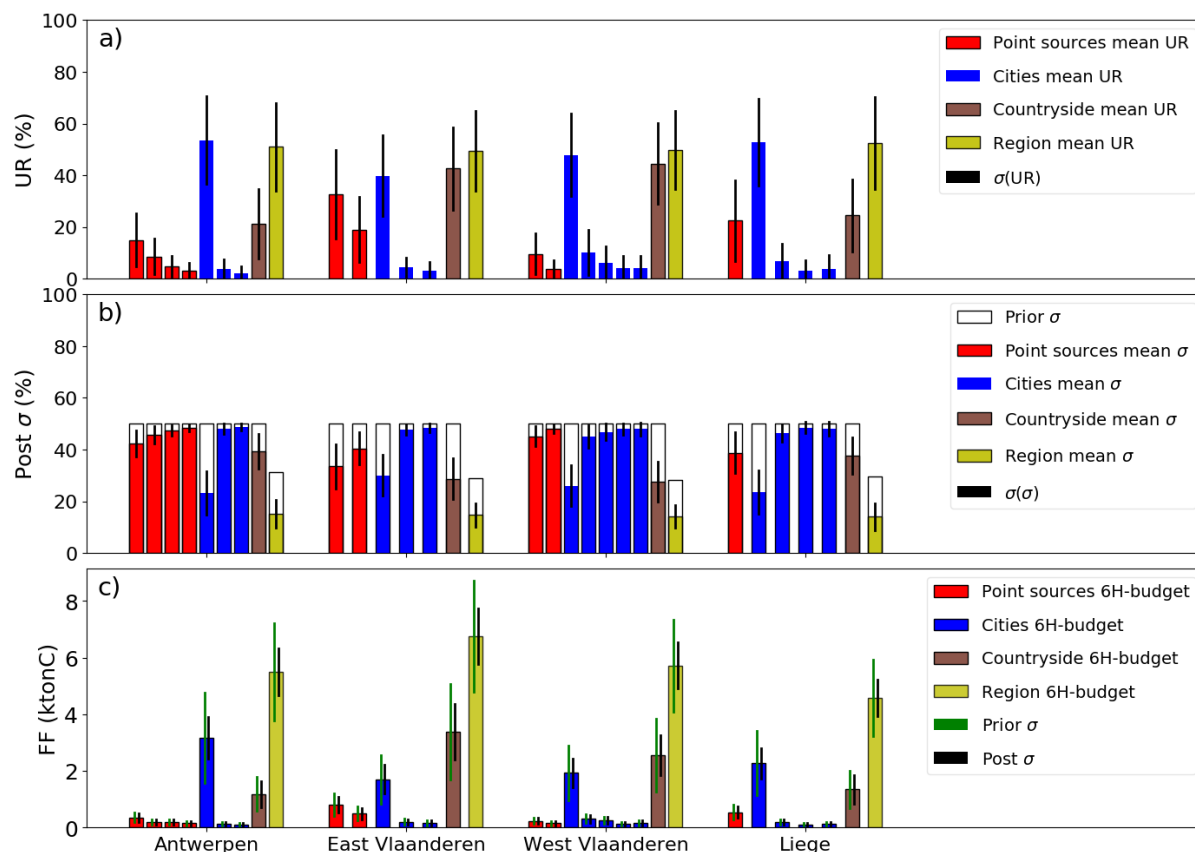


Figure 8: (a) Mean values and standard deviations of the Uncertainty Reductions (UR) for the regions, point sources, urban and countryside areas constituting 4 Belgium regions. Averaging is performed across the 62 inversion results of the days of March and May 2016. (b) Mean values and standard deviations of the relative post uncertainty for each emitting area. Prior uncertainties are represented as well. Prior uncertainties in the regional budgets are derived by aggregation of the prior uncertainties of their constituent emitting sources (mean value ~33%). Panel (c) shows the mean 6-hours budgets for each emitting area. The inversions are performed with a retrieval resolution of $2 \text{ km} \times 2 \text{ km}$, a precision of 0.6 ppm and a swath of 900 km. Prior uncertainties on the 6h-budgets of the point sources, urban and countryside areas are taken equal to 50% and prior error correlations between hourly emissions have a temporal length of 3 hours.

995

1000

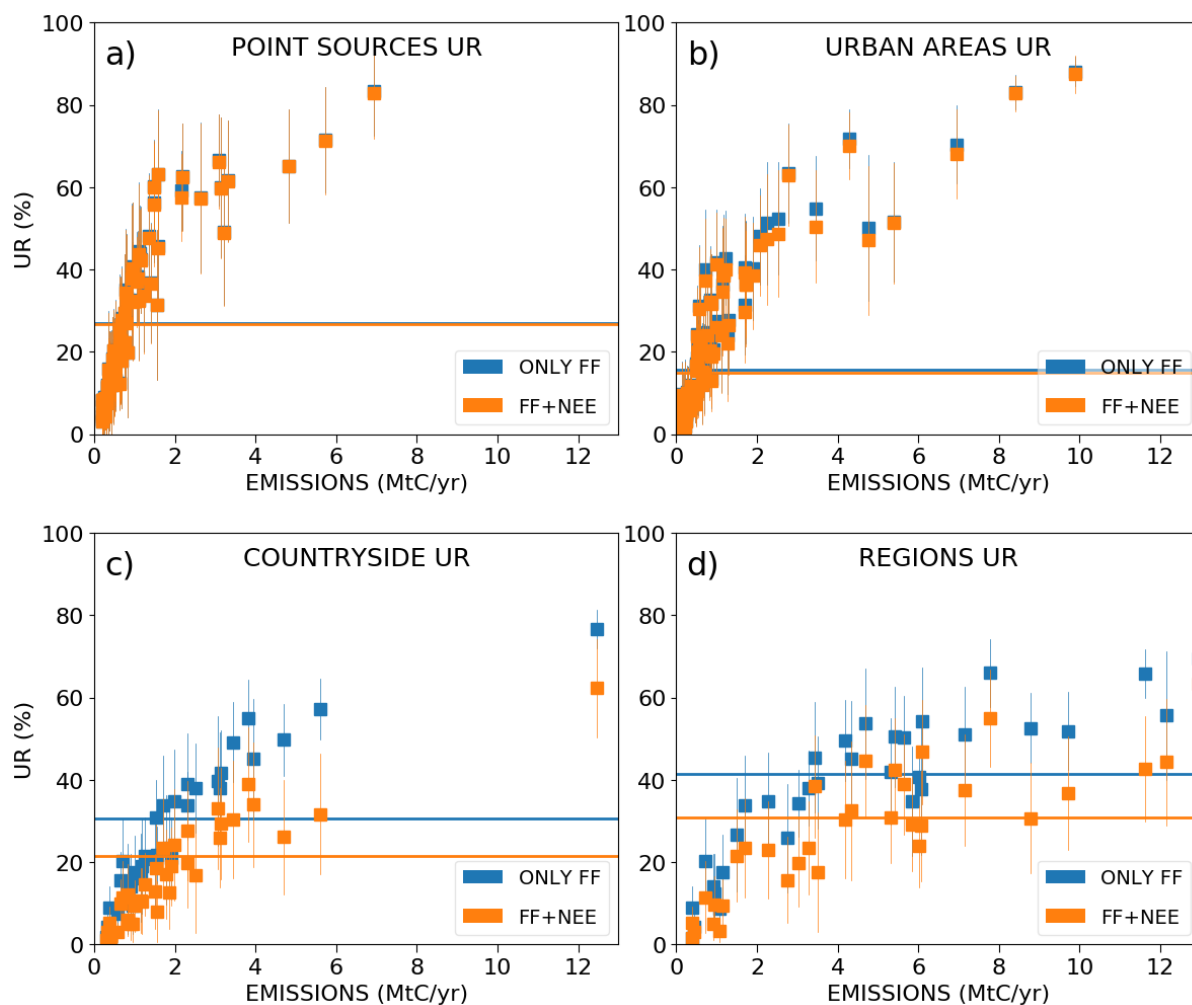
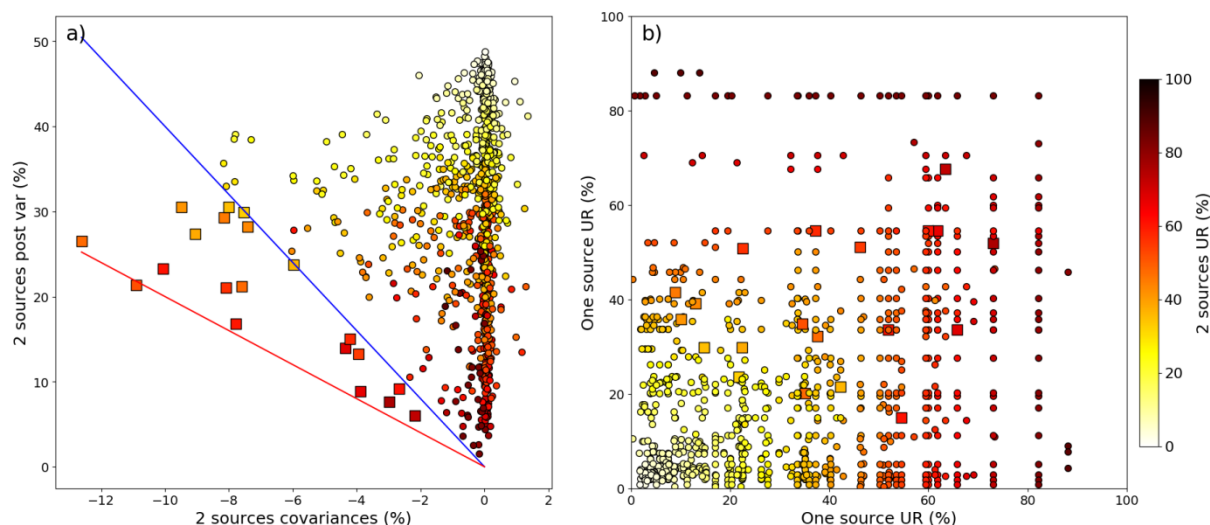
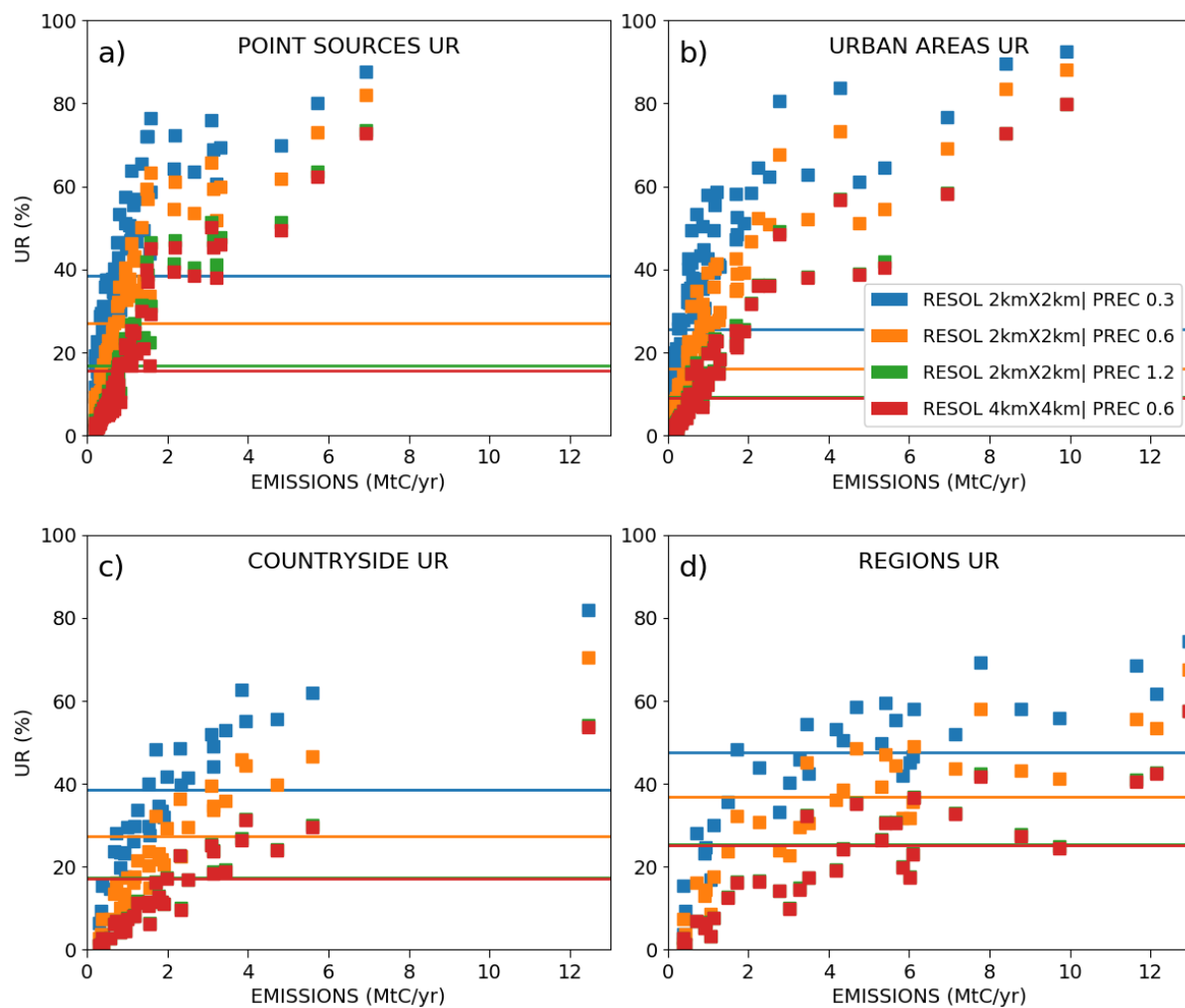


Figure 9: Same as Fig. 7 but results are derived from inversions considering the anthropogenic emissions only (blue markers) and from inversions considering the natural fluxes as well (orange markers). Prior uncertainties on the 6 h-budgets of the point sources, urban and countryside areas are taken equal to 50% and prior error correlations between hourly emissions have a temporal length of 3 hours. Prior uncertainties on the regional budgets are then derived by aggregation of the prior uncertainties of their constituent emitting sources (mean value ~33%).

1005



1010 **Figure 10: a) Post variances of the emission estimates for pairs of anthropogenic sources contained within a same region function**
of the covariances between the individual sources of the pairs. The colors of the markers correspond to the UR of the pairs. b) For
a pair of anthropogenic sources contained within a same region, UR of one individual source function of the UR of the other
individual source of the pair. The colors of the markers correspond to the UR of the pairs. The regions corresponding to this plot
are contained within the 2 km-resolution area of the model. Results are derived with an instrumental resolution of 2 km × 2 km, a
precision of 0.6 ppm and a swath of 900 km. Prior uncertainties on the 6 h-budgets of the point sources, urban and countryside
areas are taken equal to 50% and prior error correlations between hourly emissions have a temporal length of 3 hours. Pair of
1015 **anthropogenic sources are made up of point sources and of urban and countryside areas**



1020 **Figure 11: Same as Fig. 7 but the inversions are performed with different retrieval resolutions and precisions (swath=900 km). Prior uncertainties in the 6 h-budgets of the point sources, urban and countryside areas are taken equal to 50%.**

1025

1030

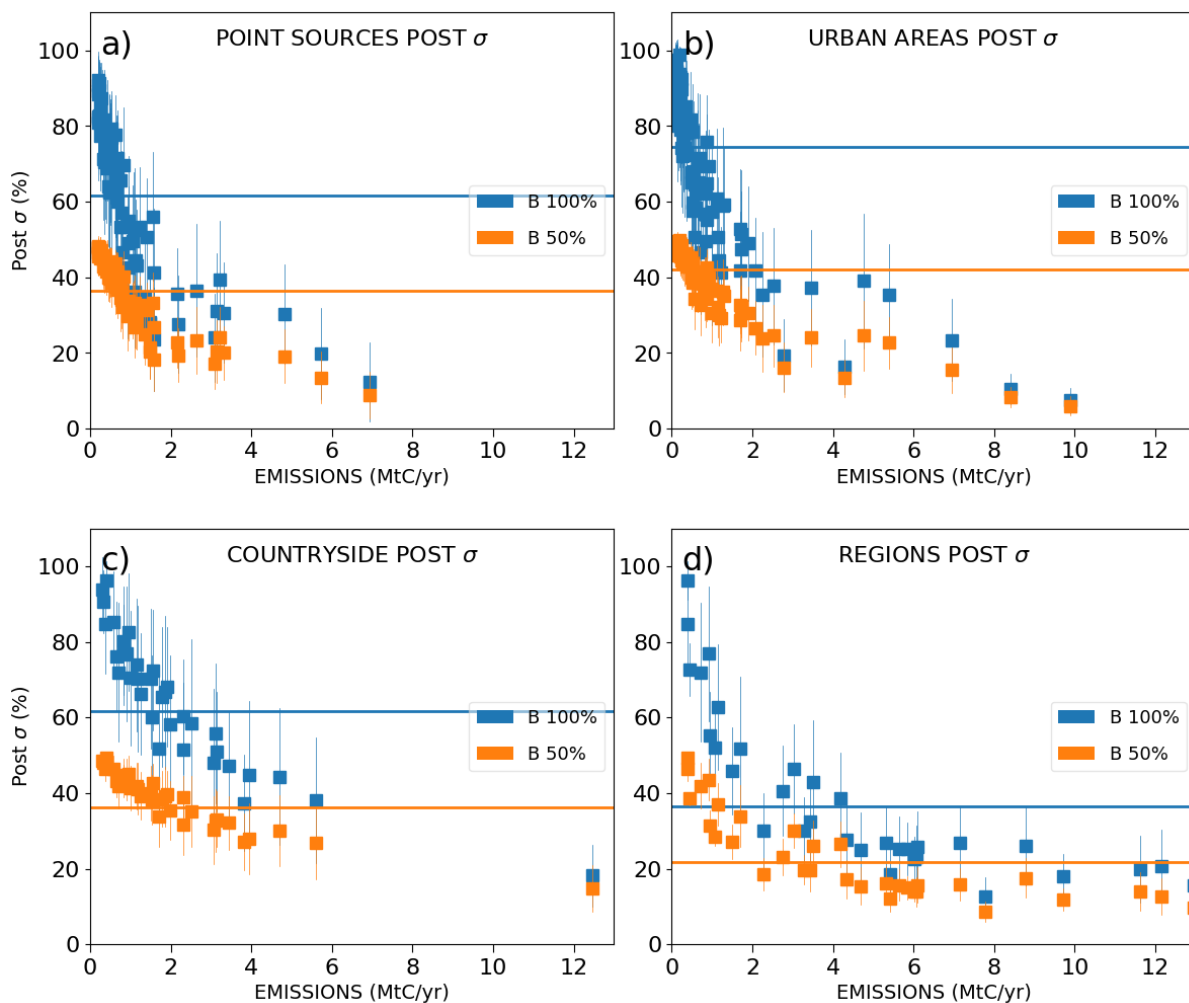


Figure A1: Same as Fig. 7 but relative posterior uncertainties are shown instead URs.

1035

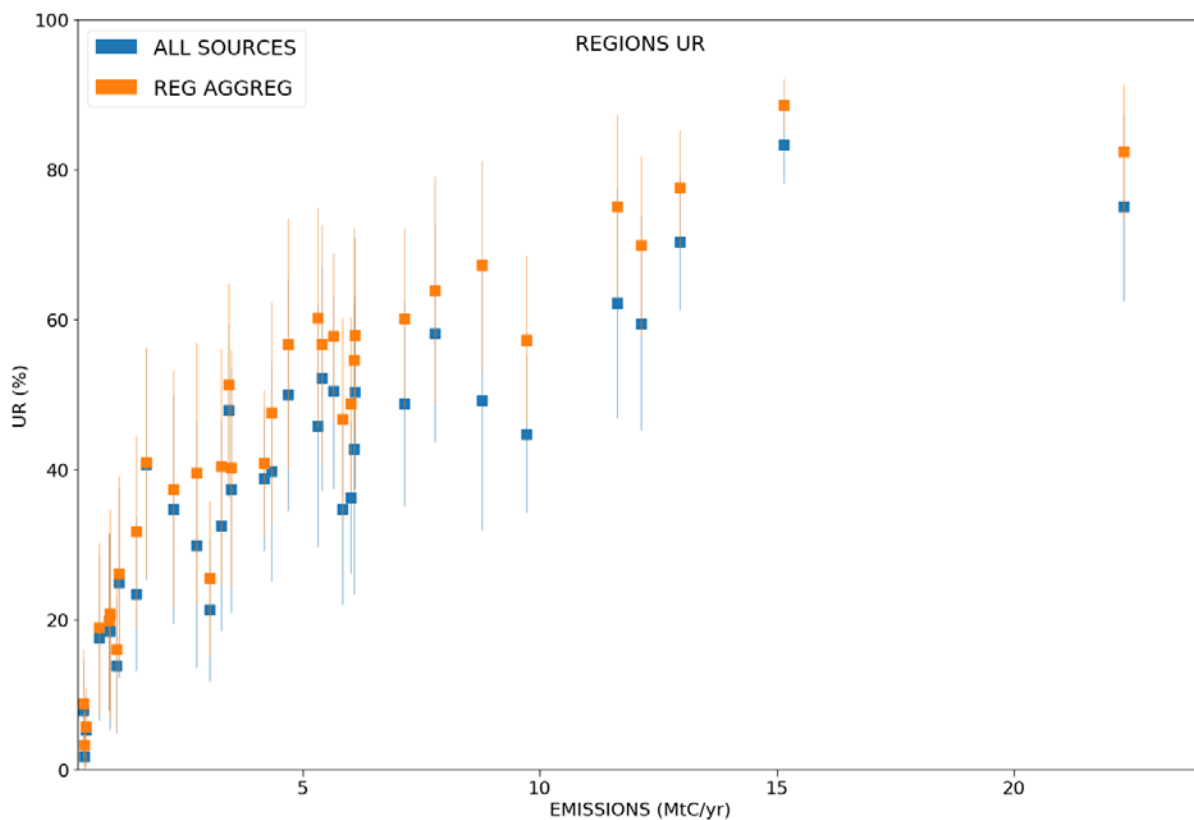


Figure A2: Mean values of the Uncertainty Reductions (UR) of the emissions at the regional scale across the 62 inversion results of the days of March and May 2016. Results are given function of the annual emissions (x-axis). Regional emissions are inverted with (blue markers) and without (orange markers) considering an internal separation of the region into cities, point sources or countryside areas.

1040